Optical Observations of Afterglows of Gamma Ray Bursts Localized by the High Energy Transient Explorer

by

Allyn Dullighan

B.A. Astrophysics (2001), Swarthmore College

Submitted to the Department of Physics

in partial fulfillment of the requirements for the degree of

Master of Science

at the

MASSACHUSETTS INSTITUTE OF TECHNOLOGY

June 2004

Author .....

Department of Physics

May 21, 2004

Certified by ..

George Ricker

Senior Research Scientist, Center for Space Research

Thesis Supervisor

Certified by .....

Saul Rappaport

Professor of Physics

Thesis Supervisor

Accepted by .....

Thomas J. Greytak

Professor of Physics

Associate Department Head for Education

Optical Observations of Afterglows of Gamma Ray Bursts Localized by the High Energy Transient Explorer

by

Allyn Dullighan

Submitted to the Department of Physics
on May 21, 2004, in partial fulfillment of the
requirements for the degree of
Master of Science

Abstract

In this thesis, I discuss observations of the optical afterglows of seven *HETE* GRBs, carried out mainly with the Magellan Telescopes at Las Campanas Observatory in Chile. Five of the bursts, GRBs 020331, 030115, 030418, 030723, and 030725, had optical afterglows. I was able to make detections of all but GRB 030115. GRBs 011212 and 020531 did not have observed afterglows, and with 030115, I can place constraining upperlimits on their optical or near infrared afterglows. For the bursts which were detected, I have constructed light curves from my data and that available from the literature in order to study the nature of these afterglows and compare them to the available theoretical models.

Thesis Supervisor: George Ricker
Title: Senior Research Scientist, Center for Space Research

Thesis Supervisor: Saul Rappaport
Title: Professor of Physics

Acknowledgments

I would like to first thank my advisor, George Ricker, for three years of scientific guidance and unwavering support, and for being understanding of my reasons for writing this thesis. I would also like to thank Saul Rappaport and Scott Burles for giving their time, knowledge, and patience to read and critique this work, and especially for their willingness to join this effort on such short notice. Thanks also to Jackie Hewitt and Deepto Chakrabarty for academic advice during my time here.

My two forerunners as HETE graduate students have been incredible mentors for me, Glen Monnelly, who guided me for my first year here while writing his own thesis, and Nat Butler, who has been an officemate and steady source of knowledge, and whose early comments jump-started this work. I have had an unforgettable experience working with the entire HETE team, working my way up from being lost among jargon at my first Ops meeting, to a part of a team glued together by cooperation, stress, and always humor. I would never have made it through this without the patient support of MOM Roland Vanderspek, who has been a 'mom' as well, the wells of knowledge Geoff Crew, Joel Villasenor, John Doty, Gregory Prigozhin, Jean Farewell, and all the HETE team members connected through 'hchat', particularly Carlo Graziani and Tim Donaghy.

Thanks to all the Astro graduate students at MIT, and those they dragged here with them, who have made this 'Institute' enjoyable, in particular, Jake Hartmann, Adrienne Juett, Matthew and Anel Muterspaugh, John Fregeau, Grace Yu, Miriam Krauss, Tesla Jeltema, Cassie and Judd Bowman, Adam and Marsha Bolton, Thandi and Mike Muno, Kristen Burgess, Bobby Conahim, Edward Boyce, Will Farr, Steve and Amy Cho, and too many more. Fridays are always a relief with this crowd, and give you a reason to work hard the rest of the week. I would also to thank all those who have filled my life away from MIT, including Gil Jones, Rodolphe Boulanger, Jesse Colman-McGill, Paul Arandia, Nicole Karluk, Magdalena Derdzinska and John Halford, and little Taka. Thanks especially to Jeff Miles, who has always been at my side, even when he is far from Boston.

Thanks to my family, my father John, who has given me his love of learning, my mother Elizabeth, who always supports me, my sister Claire, who listens and laughs, and Page, Charlie and all the Evetts for teaching me their wonderful perspective on life. Finally, thanks to my grandparents, Mary, Barbara, and Bill who have inspired and molded me in so many ways.

Contents

List of Figures

List of Tables

Chapter 1

Introduction

1.1 Gamma Ray Bursts

1.1.1 The History of GRBs

Gamma Ray Bursts (GRBs) were first detected by the Vela satellites in the late 1960s and early 1970s. This constellation of satellites was launched in order to observe the Earth and the moon for illegal detonations of nuclear weapons, which were banned by international treaties. The satellites mainly observed in the gamma-ray energy bands, as it was thought that the only sources for this radiation would be man-made nuclear explosions (and the sun). Instead, the satellites detected short bursts of radiation from random directions in the sky. The bursts were localized through triangulation among multiple satellites. None were seen to repeat, and they did not come from any specific locations, such as the moon or a satellite in a higher orbit. These results were reported to the scientific community by Klebesadel, Strong & Olson (1973), and the science of GRB astronomy was born.

During the 1980s, a number of gamma-ray instruments were launched on interplanetary missions, including the Gamma Burst Detector on the Pioneer Venus Orbiter (Klebesadel et al., 1980), the Gamma Ray Spectrometer on the Solar Maximum Mission (Harris & Share, 1998), and the KONUS instruments on the Venera missions (Mazets & Golenetskii, 1981). These instruments could localize bursts either through triangulation with other satellites, or through angular dependent responses of multiple detectors such as in the KONUS experiments. The gamma ray emission was studied, but there was not a large enough sample to make any broad generalizations. In particular the distance scale of the bursts was not known, and GRBs were hypothesized to originate anywhere from inside the solar system to distant galaxies. The large flux of gamma rays from each burst ($\sim 10^{-4}$erg/cm^2), outshining all gamma ray sources except the sun, implied a huge energy release if the sources were in fact extra-galactic.

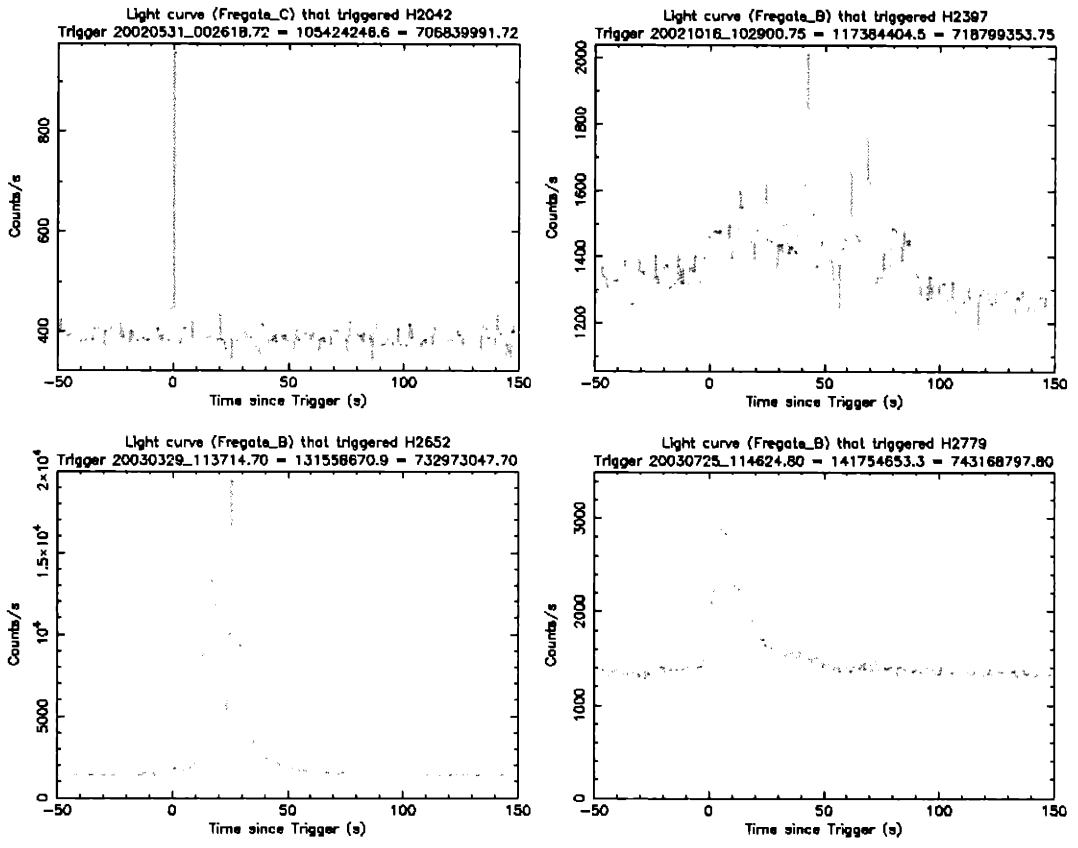

Figure 1-1 Examples of *HETE* detected GRB lightcurves are shown. Clockwise from top left, the Short GRB 020531 (H2042), a single spike with T_{90} of 1.15 seconds, GRB 021016 (H2397) shows many spikes of varying flux, GRB 030329 (H2652) has two faint peaks followed by two bright peaks, and GRB 030725 (H2779) is an example of a simple FRED.

The Burst and Transient Source Experiment

The first instrument designed to observe GRBs in detail was the Burst and Transient Source Experiment (*BATSE*) (Meegan et al., 1996) on NASA's Compton Gamma-Ray Observatory (*CGRO*), launched in 1991. *BATSE* consisted of 8 identical detectors mounted on the corners of the *CGRO* so as to continuously monitor the full range of viewable sky from any spacecraft orientation. The low earth orbit of the spacecraft restricted the field of view to 2 steradians. *BATSE* had the ability to localize bursts to within a few degrees by comparing the flux from the multiple detectors, but its primary goal was to obtain detailed lightcurves and spectral information for each burst detected.

The spectral information from *BATSE* led to a model of the standard burst spectrum. The Band Model (Band et al., 1993) describes the gamma ray spectrum of a GRB as a broken power-law with a break energy of E_0. The low energy regime is fit by a power-law with an exponential cut-off, $N_E(E) \propto E^{\alpha} e^{-E/E_0}$, and for energies

above E_0, the spectrum is a pure power-law, $N_E(E) \propto E^\beta$ where $\alpha > \beta$.

A major result from *BATSE* was the determination that GRBs are distributed isotropically on the sky (Briggs et al., 1996, Figure 1-2). This finding ruled out a number of Galactic theories. Galactic disk sources, such as neutron stars, would be concentrated towards the Galactic plane and would not appear isotropic. The same is true for sources in the plane of the solar system. However, a Galactic halo population, or even isotropically distributed, low luminosity sources near the Sun, could not be excluded. Another piece of evidence for the cosmological nature of GRBs was the apparent lack of low flux bursts.

The next step was to find optical counterparts to these high energy sources, to see what kind of objects they were associated with. In particular, optical spectra would hopefully contain emission lines from the source, or absorption lines from intervening matter, and so set the redshift of the source. It was predicted (Mészáros & Rees, 1993; Katz, 1994) that a transient optical source would be visible for each GRB, but without a distance scale a magnitude could not be estimated. The ~2 degree error circles from *BATSE* were much too large for deep optical searches, however, and no bright transients were ever discovered in wide field observations.

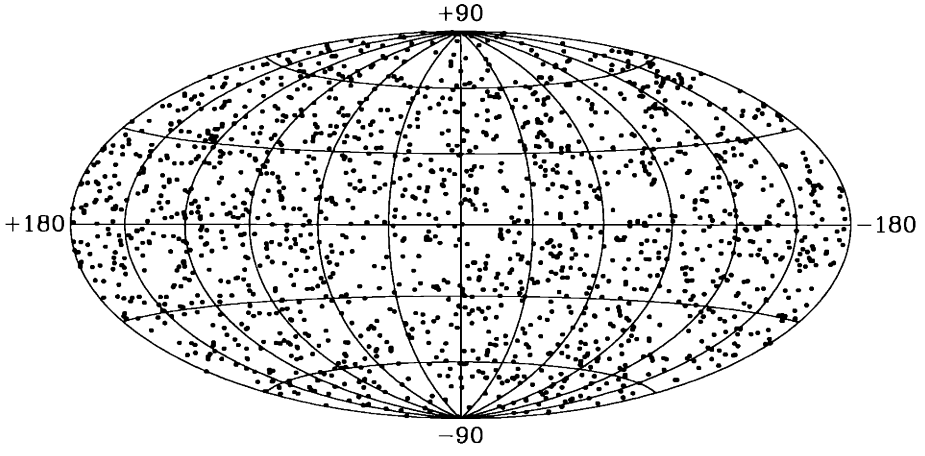

Figure 1-2 The *BATSE* instrument on the Compton Gamma-Ray Observatory localized GRBs to within a few degrees and they were seen to be distributed isotropically on the sky. This finding potentially eliminated Galactic or solar system sources for the bursts (Paciesas et al., 1999).

Studies of the First *BATSE* Catalog of GRBs also showed a distinct bimodal distribution of burst duration, with a break at about 2 seconds (Kouveliotou et al., 1993) (Figure 1-3). Kouveliotou et al. (1993) defined GRB durations in terms of T_{50} and T_{90}, the times over which 50% and 90% of the counts were detected for a burst. The "Short" GRBs have an average T_{90} of about 0.2 seconds and generally harder spectra than the Long group. Both groups have isotropic distributions and similar peak flux distributions. Long GRBs make up about three quarters of all GRBs detected in gamma-rays and all of those that have been detected at longer wavelengths. The traditional Long GRB has an average T_{90} duration of ~20 seconds

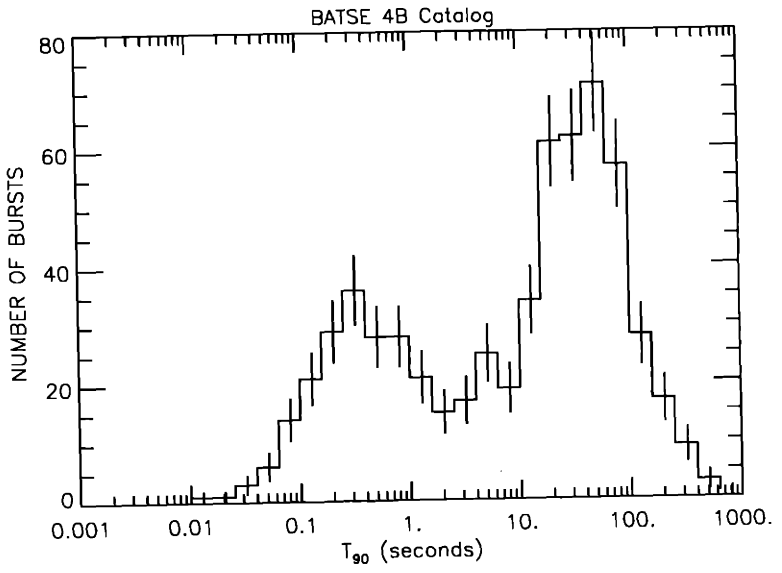

Figure 1-3 This histogram from the Fourth *BATSE* Gamma-Ray Burst Catalog (Paciesas et al., 1999) shows the bimodal distribution of Long and Short GRBs.

and a variable lightcurve. Peaks in the emission of both groups can often be described with a Fast Rise, Exponential Decay (FRED) (Fishman & Meegan, 1995) shape of varying length, although there are many exceptions. A few examples of GRBs detected by the *HETE* satellite (Section 1.3) are shown in Figure 1-1.

1.1.2 The Fireball Model of GRB Emission

The 'fireball' model (Rees & Mészáros, 1992) describes the prompt GRB emission, and has successfully predicted and described the afterglow emission (Section 1.2) from "Long" GRBs as well. The relativistic fireball used in the model is created through radiation energy injection of $E_f \sim 10^{51}$ergs by a compact progenitor (Section 1.1.5). Initially, the energy density will be so high that any matter contamination will make the fireball optically thick, and the radiation energy will be converted into kinetic expansion energy. Assuming that the fireball expands into a cool, thin external medium, a shock front will be created at the boundary and will move outwards with Lorentz factor Γ_f. Expanding adiabatically, the fireball will cool and its density will decrease in the comoving frame, until it becomes optically thin at the "deceleration radius", r_{dec}. At this point, the kinetic energy will be reconverted back into radiation. The time scale for radiative cooling ($< 10^3$ seconds in the comoving frame) is compressed in the observer's frame to $\sim r_{dec}/2\Gamma_f^2 c$ (Rees & Mészáros, 1992), giving a burst of radiation in a few seconds. The spectrum of the radiation is similarly boosted, converting keV photons in the comoving frame to MeV photons in the observer's frame. Lorentz beaming of the radiation also takes place, leaving only a small solid angle, $\sim \Gamma_f^{-1}$, observable outside the comoving frame. Therefore, a geometrically beamed fireball with $\theta_f > \Gamma_f^{-1}$ would not be distinguishable from an isotropic fireball in the

prompt emission. Finally, the external shock front loses much of its energy at the deceleration radius, but is still quite energetic. It will continue to cool long after the prompt burst and create the decaying afterglow radiation seen at longer wavelengths.

The variable lightcurves of GRBs (Figure 1-1) imply that a homogenous fireball with a single, smooth shock front cannot be the case for all events. Inhomogeneous energy injection by the progenitor could create a series of expanding shells, each with a different Γ (Rees & Mészáros, 1992). Later shells will catch up with earlier shells, either as the early shells decelerate near the external shock, or if the later shells start with a higher Γ. Each collision will decelerate a shell and convert some of its kinetic energy into a radiation burst. Multiple bursts would combine to create the total observed prompt lightcuve.

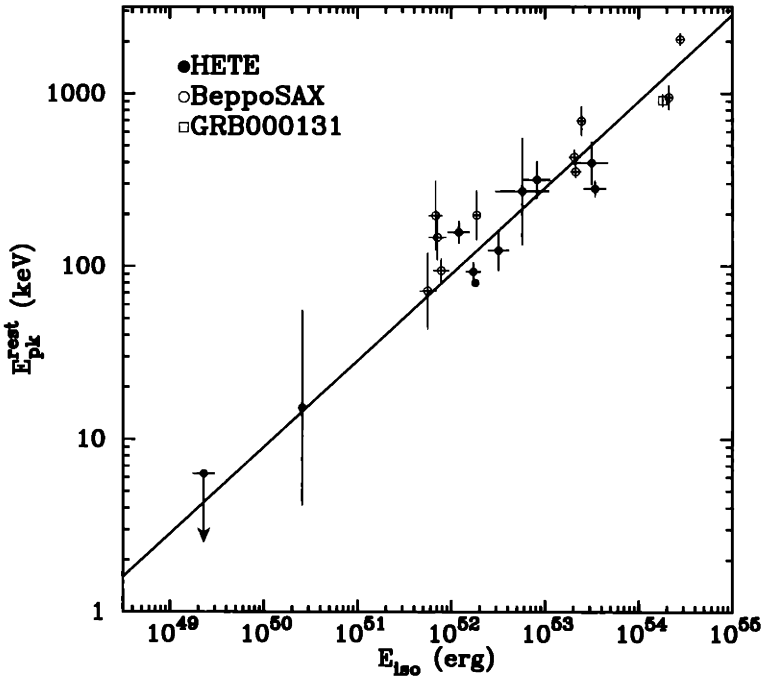

Figure 1-4 The Amati relation (Amati et al., 2002) is the correlation between the peak spectral energy in the rest frame of the burst, E^{rest}_{peak}, and the isotropic equivalent energy, E_{iso}= $4\pi r^2(1+z) * Fluence$. Two *HETE* XRFs, 020903 and 030723, have extended this relation by two orders of magnitude into the low E_{peak} regime, and shown that, so far, XRFs are consistent with an extension of the GRB spectrum. (Lamb et al., 2004a)

A number of empirical laws have been defined for GRBs in an effort to stimulate theory. The Amati relation (Amati et al., 2002, Figure 1-4) is defined as the peak spectral energy of the prompt emission in the burst rest frame, E^{rest}_{peak}, versus the isotropic equivalent energy, E_{iso}= $4\pi r^2(1+z) * Fluence$. E_{iso} assumes that the GRB fluence is equal in all directions and, as evident in Figure 1-4, ranges from 10^{49} to 10^{54}ergs for GRBs with known redshifts. When the first redshifts were found, and the cosmological distance scale of GRB understood, this energy scale had to be

accounted for. The variability ($\sim$ milliseconds) of prompt GRB emission sets the size scale of a progenitor to approximately stellar through $\delta\ tc$, and the rest mass of a star is 10^{54}ergs. This pushes the energy released in bright GRBs much too close to the total energy reservoir, but if the emission were collimated into narrow jets, the energy release would drop significantly. Jets are not uncommon among astrophysical objects, often resulting from the interactions of accretion flows and the strong magnetic fields in compact objects (pulsars, quasars, Active Galactic Nuclei, etc.). In the case of GRBs, they quickly became part of the standard model.

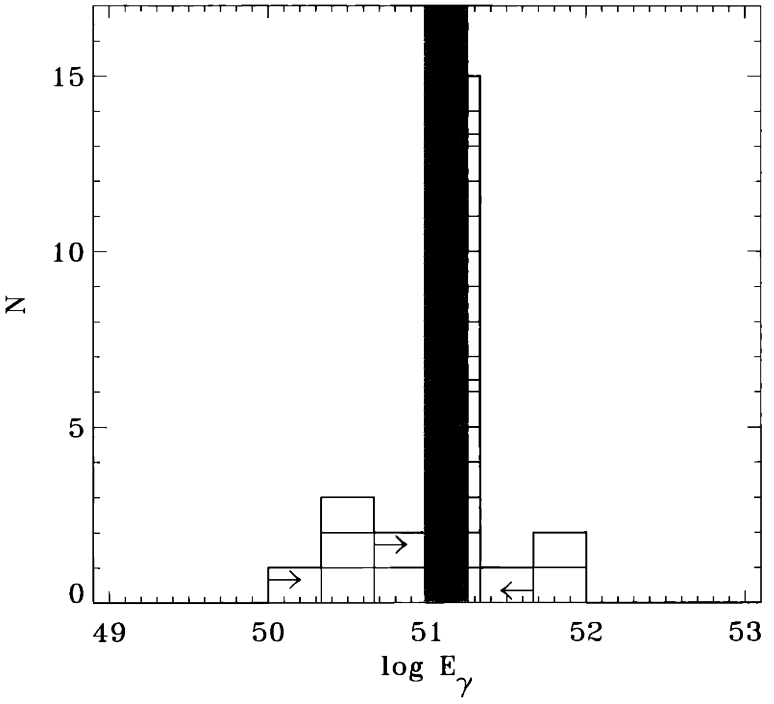

Figure 1-5 The energy released by a collimated GRB is $E_\gamma \sim E_{iso} * \theta_j^2/2$ for a jet opening angle of θ_j. The equivalent isotropic radiation from GRBs has a wide spread (Figure 1-4) but when corrected for jet opening angle, this range narrows significantly. (Bloom, Frail, & Kulkarni, 2003)

1.1.3 GRBs and Jets

The uniform jet theory (Rhoads, 1997, 1999) assumes a top-hat density structure, with the collimated region having uniform density and energy out to a cutoff angle, θ_j. For a uniform jet model, a GRB looks the same from any viewing angle inside the jet opening angle, and is not visible from larger angles due to relativistic collimation. Using the uniform jet model, the total energy of a burst can be calculated if the jet opening angle and distance are known. Surprisingly, correcting for jet opening angle (calculated from the afterglow, Section 1.2.1), narrows the distribution of total energy in the prompt emission to a sharp peak at 10^{51}ergs (Bloom, Frail, & Kulkarni,

2003, Figure 1-5), suggesting a standard energy reservoir for GRBs. When combined with the Amati relation, the uniform jet model seems to create GRBs where wide jets produce soft events and narrow jets produce harder events.

Other theories have introduced more complex "structured" jets to explain the E_{iso}, E_{peak} relation. Well studied examples include gaussian or other smoothly varying shapes (Mészáros, Rees, & Wijers, 1998; Zhang et al., 2004). In these theories, similar jets can produce a wide spectrum of prompt emission. As energy density and Lorentz factor fall off towards the edges of the jet, the viewing angle of the observer produces GRBs with a range of flux and E_{peak}. Recently, a double jet structure has been hypothesized to explain specific afterglow rebrightening features (Figure 1-8). The double jet consists of a narrow, highly relativistic inner jet with a slower, wider jet surrounding it, and seems to model a few examples very well (Berger et al., 2003; Huang et al., 2003).

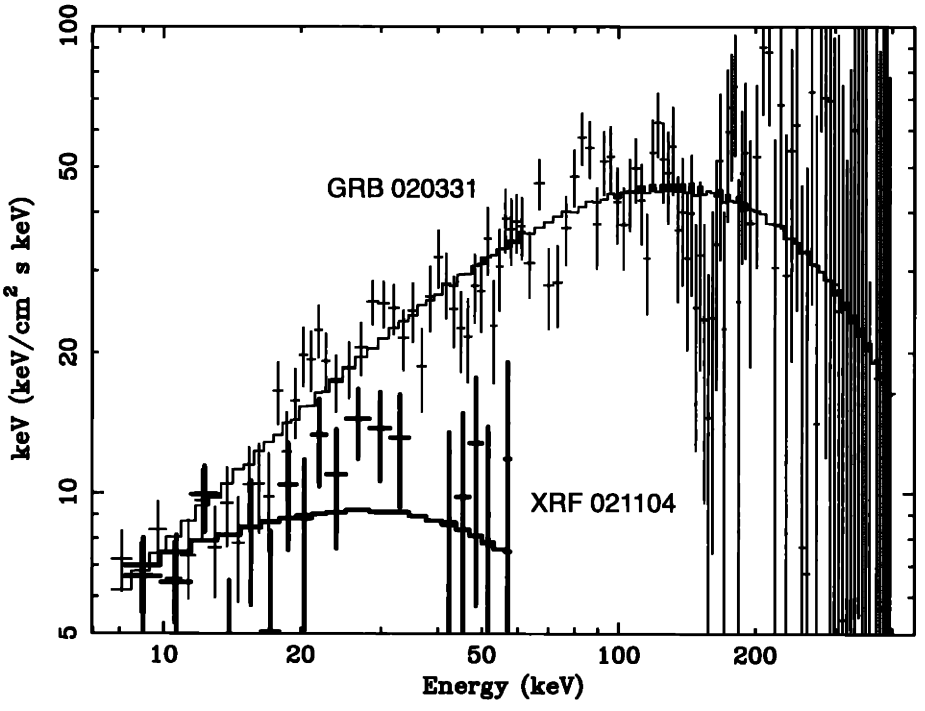

Figure 1-6 Band model fits to the spectrum of a typical Long GRB and an XRF. The XRF spectrum is much softer, with similar flux in the X-rays (< 25 keV), but very little above 50 keV. Figure adapted from Barraud et al. (2003).

1.1.4 X-Ray Flashes

X-Ray Flashes (XRFs) are a subset of Long GRBs with much softer spectra, making up about 25% of the Long GRB population and about 30% of all localized

HETE bursts. The prompt emission of an XRF is similar in all respects to the Long GRB group, except for their spectra, which have E_{peak} less than 50 keV (Barraud et al., 2003), whereas the average Long GRB has an E_{peak} ~200 keV (Preece et al., 2000). *BATSE* did not trigger on any XRFs because the energy range of its detectors did not extend below 25 keV, where most XRF prompt emission lies. The X-ray (2-25 keV) detectors used by *BeppoSAX* (Section 1.2) for localization increased its sensitivity to XRFs, but as the population was not recognized (Heise et al., 2001; Yamazaki, Ioka, & Nakamura, 2002) until late in its mission, its triggers were not optimized for this energy range. Two XRFs, 011030 and 020427, detected near the end of the *BeppoSAX* mission, were the first XRFs to have afterglows detected and host galaxies observed. Both bursts had X-ray afterglows which were coincident with small, starforming galaxies. Photometric redshift limits (z<3.5) were placed on their host galaxies (Bloom, Frail, & Kulkarni, 2003). *HETE* can trigger on its X-ray detectors, which has dramatically increased the rate of XRF localizations reaching the community. Two *HETE* XRFs have had optical afterglow detections and redshifts, XRFs 020903 (z=0.25) (Soderberg et al., 2002b), and 030723 (z<2.1) (Fox et al., 2003b; Fynbo et al., 2003a, Section 2.7).

A unified theory of GRBs and XRFs could stem from a number of possible links between the two groups. Some XRFs could be high redshift, classical GRBs (z>6) (Heise et al., 2001), but this cannot be the case for all XRFs, as the four with detected afteglows all have z<3.5. Alternatively, XRFs could be related to GRBs through the nature of their jet emission (Section 1.1.3). If the Lorentz factor, Γ, of the outflow is lower in XRFs than in GRBs, the spectrum of the prompt emission from shocks in the jet would be similarly redshifted. For example, a jet with higher matter density would consume more energy per solid angle to drive Γ in the outflow. Models of relativistic outflows predict that XRFs would be produced from a jet with $50 < \Gamma < 200$, whereas jets producing GRBs would have $200 < \Gamma < 400$ (Dermer, Chiang, & Bottcher, 1999). Yamazaki, Ioka, & Nakamura (2002) suggest that a classical GRB "uniform" jet seen from outside the geometric collimation angle would yield an XRF prompt event. By splitting the outflow velocity into radial and tangential pieces, the portion of the outflow visible to the observer has relatively lower Γ. The flux from such a burst would be very faint, as most of the radiation is beamed into the main event. These bursts may account for a population of low redshift (z<0.4) events, however, because they are visible from wide angles. Finally, structured jets, as discussed in Section 1.1.3, can easily produce XRFs, as the Lorentz factor in the outflow is dependent on the angle from the axis and therefore dependent on the angle of the observer.

1.1.5 Long GRB Progenitors

Theories on the progenitors of Long GRB have at this point only indirect constraints, mainly through the fireball emission, although recently many details have fallen into place. The huge energy release ($\sim 10^{51}$ergs), over short time scales was the first aspect to be modeled successfully. As described in Section 1.1.2, variability in GRB lightcurves, even when the high Lorentz factors are taken into account, restricts the size of the emitting region to a stellar system, and the progenitor of the radiating

jet must be proportionally smaller still. GRBs being the result of core collapse in a massive star was first suggested by Woosley (1993), under the guise of a "failed" supernova (SN) where the core of the star collapses into a BH, but the outer layers are accreted instead of ejected. The "failed" SN may not actually fail, as described in the "collapsar" model (MacFadyen & Woosley, 1999; Zhang, Woosley, & MacFadyen, 2003). The binding energy of the accretion disk or BH rotational energy, extracted through magnetic field interactions, may be enough to eject the outer layers. Either mechanism may cause a GRB, beginning about 10 seconds after the inner core of the star collapses into a BH, during which time material at the poles of the BH fall in and the rotating equatorial regions form an accretion disk. The empty polar regions channel the outflow powered by the BH-disk system into jets, which punch through the remaining outer layers of the star. Once the jets are free of the star, the fireball regime begins and a GRBs is created (Section 1.1.2). The accretion rate can be very unstable, creating multiple short bursts of energy injection, which then create multiple shells to later collide in internal shocks in the jet (Zhang, Woosley, & MacFadyen, 2003). Recent direct evidence tying GRBs to simultaneous SNe (Section 1.2.4), was found in the afterglow of GRB 030329. A SN lightcurve and spectrum was seen to rise above the GRB afterglow light at about 10 days after the burst, which would be expected if a collapsar had created the burst.

The GRB may also occur from weeks to months after the SN, according to the "supranova" model (Vietri & Stella, 1998), if a supra-massive neutron star (NS) is formed from the SN. This NS would be over the mass limit for stable neutron degeneracy support, but spinning rapidly enough to support itself against further collapse. As the NS spins down it will become unstable. The core will collapse into a BH and accrete the outer layers, triggering the GRB. The prompt GRB emission would not be strongly affected by the collapse timing with respect to the SN, but the interactions between the external shock and the interstellar medium which create the afterglow would be affected. The stellar material ejected by a SN occurring months before the GRB would be driven out by the NS wind into shells surrounding the star. The external shock would either move through these shells and interact with them, or if enough time had elapsed and they were relatively distant, heavy metal absorption should be present in the afterglow spectrum. A few suggestive metal lines have been seen in X-ray spectra of GRB afterglows (Reeves et al., 2003; Butler et al., 2003a), but their significance is low.

1.1.6 Short GRBs

It is thought that Short GRBs are produced when compact NS binaries (NS-NS, or NS-BH) coalesce (Narayan, Paczynski, & Piran, 1992). As the coalescence begins, the smaller NS will be torn apart by tidal forces and accreted onto its companion. A fireball (Section 1.1.2) is formed and collimated by the magnetic field of the BH-torus system, and the GRB radiation is emitted through internal shocks, similar to Long GRBs. The accretion is rapid, but the fast and variable lightcurves also result from relativistic effects. It is likely that these binaries would have traveled far from dense star formation regions, because of the asymmetrical kick expected during their

formation, and the long time scale ($\sim 10^9$ years) between formation and coalescence. Traveling out of the plane and into the halo of their host galaxy, the surroundings of the binary would be relatively clean and the resulting external shocks from the jets would be very faint. This scenario would explain the lack of optical afterglow detections for Short GRBs.

Short Gamma Ray Bursts are still an enigma, with few advances in our understanding since their differentiation from Long GRBs (Section 1.1.1). Since the end of the *BATSE* mission, most Short GRB localizations have been derived by the Interplanetary Network (IPN), leading to long delays between the prompt event and the dissemination of a small error box. IPN locations are made through timing triangulation between distant satellites. The usual time lag for data transfer and analysis is days (Hurley et al., 2002a), but it can be weeks before a small error region (a few square arcminutes) is published. *HETE* (Section 1.3) is able to detect Short GRBs, but with the exception of GRB 020531, the combination of hard spectra and short durations produce too few photons below 25 keV for localizations.

1.2 Afterglows

GRBs were hypothesized to have longer wavelength emission before it was observed (Mészáros & Rees, 1993; Katz, 1994)., but the error boxes for GRB localizations from *BATSE* and other gamma-ray detectors were much too large for deep optical searches. This changed in 1997 when the Italian-Dutch satellite, *BeppoSAX* , detected GRB 970228 (Costa et al., 1997a; Groot et al., 1997). *BeppoSAX* was the first satellite to use X-ray emission to directly localize GRBs with its Wide Field Camera (WFC). GRBs were localized in the 2-30 keV band to an error radius of 3′by ground analysis. Commands could then be sent up to slew the satellite towards the GRB position, and examine the burst in the soft X-rays with its higher resolution Narrow Field Imager. It found a fading X-ray source with a 50″ error radius (Costa et al., 1997b). Optical and radio observations inside this smaller circle had many fewer background sources to contend with and a fading source was observed in both of these regimes. As the afterglow faded away, an underlying galaxy was revealed, and its redshift was measured to be 0.695 (Djorgovski et al., 1997). The association of GRB 970228 with the galaxy seemed strong, but it could have been a coincidence. The next *BeppoSAX* burst with an optical afterglow, GRB 970508, had a spectrum taken of its early afterglow, and when a redshift of 0.835 (Metzger et al., 1997) was measured for the afterglow itself, the cosmological nature of GRBs was confirmed.

1.2.1 The Standard Model

The basic model for afterglow emission from gamma ray bursts over a wide range of frequencies and times, as derived from the fireball model (Section 1.1.2) was laid out by Sari, Piran & Narayan (1998). Afterglow emission is modeled as synchrotron radiation from accelerated electrons in the external shock, formed between the GRB jet and either the stellar wind or interstellar medium. Initially, the expanding material

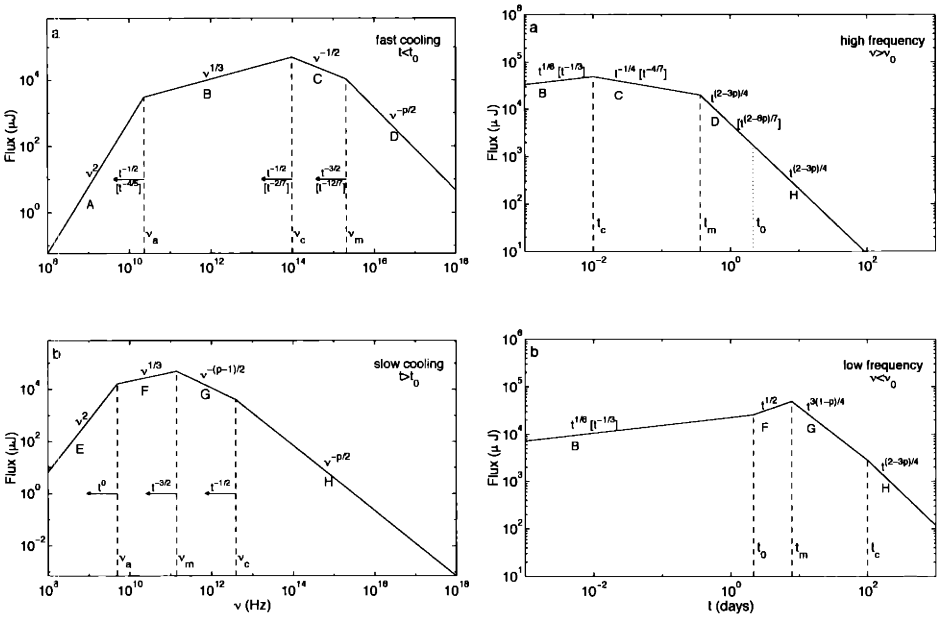

Figure 1-7 The canonical afterglow spectra and lightcurves from Sari, Piran & Narayan (1998). *Right panel*: The upper spectrum is for the fast cooling regime, and the lower is for the slow cooling regime. *Left panel*: The upper lightcurve is for the X-rays and the lower is the standard fade in the optical, not including the effects of relativistic collimation and the jet break.

in the jet is still ultra-relativistic ($\Gamma_{jet} > 100$) as it collides with the surrounding gas. The minimum Lorentz factor of the electrons, γ_m, is greater than the critical Lorentz factor γ_c, and the material is in the fast cooling regime. Each electron cools efficiently until its $\gamma = \gamma_c$. When $\gamma_m = \gamma_c$ (at time, t_0), the shock moves into the slow cooling regime. The broadband spectra for these two regimes are shown in Figure 1-7, on the left. The frequency for which the spectrum peaks at t_0, ν_0, is usually between the X-ray and optical, and the peak energy moves to lower frequency with time. The afterglow lightcurves for high energy ($\sim$ X-rays) and low energy ($\sim$ optical, IR, radio) radiation are shown on the right.

The simplest GRB late time afterglow lightcurve consists of a continuous power-law decay ($F \propto t^{-\alpha}$), but often bursts are better fit by a broken power-law curve, with the first decay usually having a slope $\alpha \sim 1$ and the second having $\alpha \sim 2$. The time of this break is hypothesized to be correlated with the opening angle of the jet, θ_{jet}, for a uniform jet (Rhoads, 1997, Section 1.1.3). Photons emitted by relativistic material with Lorentz factor Γ are collimated into a cone of angle Γ^{-1}. This restricts the visible region of the jet during the early afterglow, when $\theta_{jet} > \Gamma^{-1}$. As the shock loses energy and Γ decreases, more of the jet becomes visible. The decreasing energy in the jet is balanced by the increasing area and this slows the apparent afterglow decay. When the full jet is visible to the observer at $\theta_{jet} = \Gamma^{-1}$, the lightcurve breaks

and begins to follow the true energy decay in the shock. Relativistic jet breaks are achromatic and have been observed in a number of GRB afterglows. Combined with the redshift and the prompt fluence, jet opening angles, assuming uniform GRB jets, have been used to measure the total energy output in the prompt burst (Section 1.1.3).

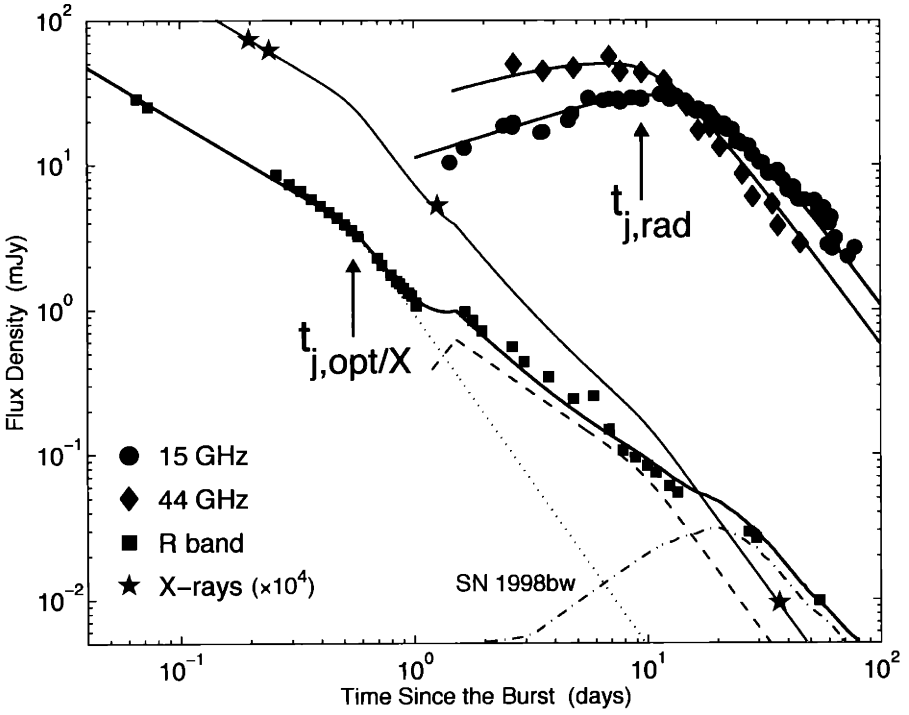

Figure 1-8 The multi-wavelength afterglow of GRB 030329 showing the standard evolution in different wavebands and the large scale departures from a smooth decay in the optical. This figure is taken from the astro-ph preprint of Berger et al. (2003).

1.2.2 Afterglows and the Two-Jet Model

GRB afterglows can have significant deviations from the single or broken power-law decay. The next step in fitting an afterglow lightcurve is looking for large scale deviations that can be fit by simple expansions to the current models. In the case of GRB 030329, shown in Figure 1-8, two major regions of excess flux have been fit in the optical (Berger et al., 2003). The dotted line shows the standard broken power law fit, the dashed line shows the first excess, fit by the two-jet model, and the dashed-dot line shows the contribution from a SN (Section 1.2.4).

The radio observations of GRB 030329 showed a clear break at about 10 days after the burst, while the optical data showed an earlier break at 0.5 days. If both these breaks are due to jet opening angles, two jets must be involved (Berger et al., 2003). The two-jet model suggests that some GRBs may have a standard, narrow, ultra-relativistic jet ($\Gamma_{narrow} \sim 300$, see Section 1.1.3) surrounded by a wider jet moving

at a slower speed ($\Gamma_{wide} \sim 30$) (Berger et al., 2003; Huang et al., 2003). Models of the optical lightcurve from on-axis show that emission from the narrow jet dominates at early times. The wide jet has a much larger area, however, so as the light from the narrow jet decays, the wide jet will begin to dominate the emission, creating a bump in the lightcurve (Figure 1-9, left panel). If the angle of the observer is outside the narrow jet, but inside the wide jet (ie, in the XRF regime, see Section 1.1.4) the observer only sees the emission from the wide jet until Γ^{-1}_{narrow} is greater than the angle of the observer (Huang et al., 2003). If the narrow jet is still bright, this can cause a sharp increase in the optical lightcurve, peaking when the narrow jet is fully visible (Figure 1-9, right panel).

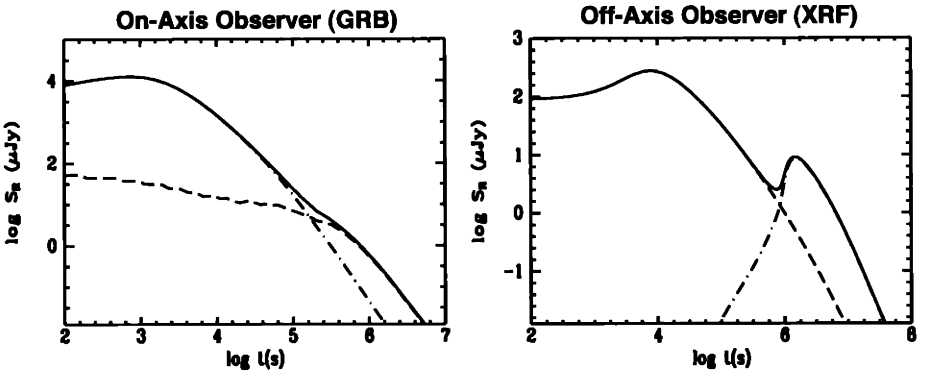

Figure 1-9 Models of two-jet GRB optical afterglows by Huang et al. (2003). In each plot the narrow jet emission is the dot-dashed line, the wide jet emission is the dashed line, and the sum of the two is the solid line. *Left panel*: For an on-axis observer, the wide jet creates a late-time flattening of the lightcurve, until it breaks at $\Gamma^{-1}_{wide} = \theta_{wide}$. *Right panel*: An off-axis observer at first sees only the wide jet, but a sharp rise at $\Gamma^{-1}_{narrow} \sim \theta_{observer}$ occurs as the narrow, more energetic jet comes into view.

1.2.3 Shells and Clumps

The two-jet model or SNe (Section 1.2.4) can only account for very specific shapes, and many afterglow lightcurves show multiple smaller rises or flattenings. The current leading theories for multiple bumps in a lightcurve usually involve inhomogeneities in either the jet or the external medium, which may cause energy fluctuations in the shock itself. The inhomogeneities can either take the form of angular clumping or radial shells, and occur in either the jet or external medium (Nakar, Piran, & Granot, 2003). Angular clumping causes fluctuations in the lightcurve as the Lorentz factor decreases and the area of the shock front visible widens to include brighter patches. Over-dense clumps in the external medium would cause regions of the jet to decelerate faster at those points and radiate their energy faster, or the jet itself could be structured with respect to angle, and as regions of higher Γ came in to view the afterglow would rebrighten. When the full jet comes in to view ($\theta_{jet} = \Gamma^{-1}$), however, angular variations must cease and the lightcurve will become smooth. Alternatively,

radial shells of over-dense regions in the gas surrounding the progenitor could cause fluctuations in the afterglow shock as the front moved out through them. Radial variation in the jet would cause similar rebrightenings, as the external shock slowed and trailing shells caught up with it, creating "refreshed shocks".

GRBs 021004 and 030329 both showed numerous rebrightening phases in their optical afterglows, on time scales of a day or more. The external shell scenario was suggested as a model for the afterglow of GRB 021004 (Schaefer et al., 2003), when spectra of the afterglow showed numerous absorption systems slightly blueshifted with respect to the redshift of the host galaxy. It is unlikely that random, unassociated systems in the host galaxy would be consistently blueshifted. More likely is that these systems are shells surrounding the progenitor, which was likely a supermassive star (Section 1.1.5) undergoing mass loss through its stellar wind. Variations in the mass-loss rate or wind speed would create shells of denser matter in the wind, and the radial velocity would blueshift absorption in the afterglow from distant shells. Closer shells create variations in the optical lightcurve as the external shock front crosses them. Schaefer et al. (2003) find that the three significant bumps in the lightcurve of GRB 021004, at 0.14, 1.1, and 4.0 days, give shells at 0.022, 0.063, and 0.12 parsecs from the progenitor, with the furthest absorbing shell at $\sim$10 parsecs, where the wind meets the interstellar medium. Studies of GRB 030329 have shown many bumps, depending on how the powerlaw decays are fit. Lipkin et al. (2004) detail clearly the obvious bumps, the first three or four of which have very similar lightcurves. This is suggestive of a similar source for each bump, and Granot, Nakar, & Piran (2003) model the bumps as refreshed shocks from radial variations in the jet outflow. The fast rise times for each bump, and the return of the lightcurve to its original decay slope after each rise indicate that the shock front is interacting as a whole during the rebrightenings. Most of these variations occur after the first lightcurve break, and if this is the jet break, angular variation cannot account for the lightcurve variations.

1.2.4 GRBs and SNe

A number of afterglow lightcurves with deep photometry have shown reddened excesses above the power-law decay at very late times (30-100 days). These "red bumps" were often consistent with a redshifted lightcurve of the unusually energetic Type IIb/c SN 1998bw (z=0.0085), which may be associated with the underluminous GRB 980425 (Galama et al., 1998). The consistent locations of GRBs within star-forming galaxies (Bloom, Kulkarni & Djorgovski, 2002) strengthened these associations, but none were conclusive. Low significance X-ray features were also consistent with heavy elements created in SNe (Butler et al., 2003a; Reeves et al., 2003), but the only conclusive connection would be an optical spectrum of a red bump, showing traditional SN emission. None of the late time red excesses were nearly bright enough for an optical spectrum, however.

Recently, *HETE* detected GRB 030329, the brightest GRB so far during its mission, and among the brightest ever detected. This GRB was not unusually energetic, but unusually close (z=0.168), and similarly its afterglow was so bright it allowed high resolution, optical spectroscopic monitoring long into its decay. At $\sim$10 days,

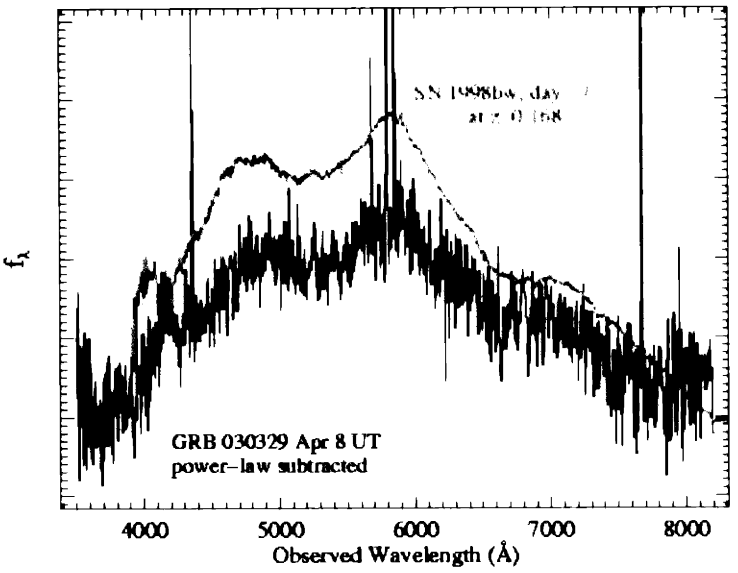

Figure 1-10 The emerging spectrum of SN 2003dh is seen in the afterglow of GRB 030329 after about 10 days. SN 2003dh is very similar to the peculiar type IIc SN 1998bw, whose wide emission lines indicate unusually high expansion velocities. Figure from Stanek et al. (2003).

when the afterglow was still at $R \sim 20$ magnitude, the optical spectrum began to show a residual emission line spectrum when the power-law synchrotron spectrum was subtracted (Stanek et al., 2003, Figure 1-10). It matched very well with the spectrum of SN 1998bw, and was officially designated SN 2003dh. The time of the initial SN explosion with respect to the peak of the lightcurve is not a well known quantity, as most SN are not found until almost at their peak. The time of the prompt gamma-ray emission in GRB 030329 is consistent to within a day of the extrapolated SN explosion time, however, suggesting they may have been simultaneous. This obviously lends support to the previous associations of red bumps in the optical afterglows of GRBs with SNe, and suggests that most Long GRBs may be created in collapsar type systems (Section 1.1.5) Recently, two XRFs with detailed late time lightcurves have also shown late time bumps consistent with SN rises (030723, Fynbo et al. (2004); 031203, Thomsen et al. (2004)), although other models for the origins of these bumps are also consistent (030723, hua03).

1.3 The High Energy Transient Explorer

The High Energy Transient Explorer satellite (*HETE*) was designed and built at MIT in collaboration with its partners at RIKEN (Japan) and CESR (France), as

a small mission to detect and localize GRBs. *HETE* was successfully launched into an equatorial orbit at an altitude of ~600 km on October 9, 2000 and has been in full operation mode since the summer of 2001. The goals of the mission are met by onboard integration of the four main instrument suites, observing in the gamma-rays, medium X-rays, soft X-rays, and optical. GRBs are detected initially in the gamma-rays (6-400 keV) by the French Gamma Telescope (FREGATE), a set of four identical scintillators collimated to a 60° radius, anti-solar Field of View (FOV). GRB localizations are made by the coded mask proportional counters of the Wide Field X-ray Monitor (WXM) in the medium X-rays (2-25 keV) , and if possible, a finer localization is produced by the coded mask CCD cameras of the Soft X-ray Camera (SXC). Finally, the spacecraft pointing is determined by the optical cameras with real-time onboard software matching the stars visible to a star catalog. Locations are quickly downlinked to the ground and relayed to the observer community through the GRB Coordinate Network (GCN) to facilitate follow up observations at other wavelengths.

1.3.1 The Satellite

HETE is a small satellite, standing only a meter high and about a meter in circumference when the solar panels are folded. The size was limited by its launch in a Pegasus rocket, which took place at the Kwajalein Air Force Base in the Marshall Islands on October 9, 2000. The satellite's near equatorial orbit (±2° of the equator) allows it to stay in constant contact with a series of ground stations sited along the equator. The three Primary Ground Stations (PGS), at Singapore, Kwajalein, and Cayenne in French Guiana, have S-band radio dishes for data uplink and downlink, which is transfered to and from MIT over the internet. The additional burst alert stations listen passively as the satellite continuously broadcasts short messages at 137.96 MHz. All of these alert stations are also connected via the internet to the MIT control center, and while in contact with the satellite they continually relay the messages back to MIT. If a burst is detected, the satellite diagnostic will change to a burst alert message, and will be sent out to the community as a GCN Notice when it reaches MIT. The onboard software calculates the position of the burst and the pointing of the satellite to the best of its ability. When the satellite next passes a PGS it will download all the burst data for further analysis by the *HETE* science team.

The highest energy photons are detected by FREGATE (Atteia et al., 2003a). Each of its four identical detectors consists of a 1 cm thick cleaved NaI crystal scintillator and a photomultiplier tube. The total collecting area is 160cm^2. The detectors are collimated to reduce noise from background sources and increase the sensitivity in its low energy range. Each photon detected is read out into a circular buffer (65536 photons long) with a tag containing its time, at 6.4 μs resolution, and energy, at 0.8 keV resolution. Until a trigger is detected, the instrument runs in survey mode, integrating counts every 0.16 seconds in four energy bands, A (6-40 keV), B (6-80 keV), C

FREGATE performances	
Energy range	6 - 400 keV
Effective area (4 detectors, on axis)	160 cm^2
Field of view (FWZM)	70°
Sensitivity (50 - 300 keV)	10^{-7} erg cm^{-2} s^{-1}
Dead time	10μs
Time resolution	6.4μs
Maximum acceptable photon flux	10^3 ph cm^{-2} s^{-1}
Spectral resolution at 662 keV	$\sim$ 8%
Spectral resolution at 122 keV	$\sim$ 12%
Spectral resolution at 6 keV	$\sim$ 42%

Table 1.1 The FREGATE performance and instrumental characteristics from Atteia et al. (2003a).

(32-400 keV), and D (>400 keV). FREGATE also generates a 128-channel spectrum of the integrated counts every 5 seconds in the range 6-400 keV. These spectra and lightcurves are downloaded during each PGS contact and used for general diagnostics and searches for untriggered events. During a triggered event, a "burst buffer" is created with more detailed information, and downloaded at the highest priority during the next PGS contact. The burst buffer contains the tagged photons starting before the burst and throughout the event.

The WXM (Kawai et al., 2003a) localizes the bursts detected by FREGATE in the 2-25 keV range, and can also trigger on its own lightcurves for soft events. The WXM consists of two pairs of Xe gas one-dimensional Position Sensitive Proportional Counters (PSPCs), each pair with a one-dimensional coded mask aperture. The two pairs of detectors are orthogonal to each other, and aligned with the X and Y axes of the satellite. The PSPCs are made up of two regions, the top having three cells with carbon fiber anode wires for counting incoming photons, and the bottom having four cells with tungsten wires for anti-coincidence rejection of charged particles. The coded mask sits 187 mm above the PSPC and incoming photons create a shadow pattern on the wires below. The position sensitive wires record an integrated Position Histogram (POS) with 1 mm resolution every 6.55 seconds for two energy bins, 2-10 keV and 10-25 keV, when in survey mode. Also, the total counts in each of the four detectors are recorded every second in four energy bands, 2-5, 5-10, 10-17, and 17-25 keV, and 32-channel pulse height spectra are recorded for each wire every 5 seconds. During a burst, tagged photons are recorded with 1 ms time, 1 mm position, and 5 bit spectral resolution (Kawai et al., 2003a). The duration that the tagged data is recorded is determined onboard, to include both the burst and sufficient background data for ground analysis.

The SXC (Villasenor, et al., 2003; Monnelly et al., 2003) can also localize bursts in its energy range of 2-10 keV. The SXC is similar to the WXM in that it has two one-

Wide Field X-ray Monitor	
Built by	RIKEN and LANL
Instrument type	Coded Mask with PSPC
Energy range	2 - 25 keV
Timing Resolution	1ms
Spectral Resolution	$\sim 25\%$ @ 20 keV
Detector QE	90% @ 5 keV
Effective Area	~ 175 cm^{2*}
Sensitivity (10σ)	$\sim 8 \times 10^{-9}$ erg/cm^2/s (2-10 keV)
Field of view (FWZM)	1.6 steradians
Localization resolution	$19'$(5σ burst)
	$2.7'$(22σ burst)

* each of two units

Table 1.2 The WXM performance and instrumental characteristics from Kawai et al. (2003a).

dimensional coded masked detectors aligned with the spacecraft axis, but the SXC uses X-ray CCDs as detectors instead of proportional counters. CCDs have much finer spatial resolution and the masks developed for the SXC take advantage of this, with 2100 coded elements over the FOV, giving typical resolution of $43''$ (90% error radius, from Monnelly et al. (2003)) over its large FOV. Typically, the SXC is used only as a vernier for WXM locations, as GRBs are much fainter in the soft X-rays. Using the $10'$ locations from the WXM significantly reduces the number of sources to exclude. Hundreds of bursts from galactic sources have been localized in this manner in order to test the system, and 15 of the 16 GRBs with SXC refined WXM locations have had afterglows discovered inside the SXC error region.

In order to be sensitive to X-rays, the CCD cameras on the SXC must have optical blocking filters. During the construction of the instrument, it was not clear how strong these filters would need to be, so two different kinds were used. The SXC was built and flown with a pair of CCDs in each detector. An outer filter of polyimide coated with aluminum covered both, and one CCD in each detector was also covered with a beryllium film (Villasenor, et al., 2003). The filters also act as protection from micro-meteor hits. Unfortunately, due to increased solar activity, atomic oxygen in the upper atmosphere was at much higher levels than expected and completely degraded the polyimide in the outer filter. The bare CCDs in each detector were destroyed a few months later as micro-meteor hits shorted the array. Currently, the Be coated CCDs are still working well, although during the six days closest to the full moon each month they receive more optical light than can be filtered out and must be turned off.

General SXC parameters	
Camera Size	100 × 100 × 100 mm
Instrument type	Coded Mask with CCID-20
Field of View	0.9 sr (FWHM)
Angular Resolution	33 ″per CCD pixel
Detector-Mask Distance	95 mm
Mask Open fraction	0.2
Mask element size	45 μm
Timing Resolution	1.2s

Table 1.3 The SXC performance and instrumental characteristics from Villasenor, et al. (2003).

1.3.2 Localizing GRBs with HETE

The FREGATE and WXM count rates are continuously monitored onboard the spacecraft with a set of trigger algorithms. If a sudden count increase is detected, and not invalidated as being due to a pre-determined effect (eg., a known X-ray source), the flight software enters a burst mode. The high resolution tagged data is saved to a "burst buffer" for downlink at the next PGS contact, and the onboard software begins to analyze the burst. Automatic localization software runs on the WXM data being collected. Similarly, locations are produced with SXC data, using the most recent location from the WXM to narrow the SXC FOV, if available. The location with the highest signal to noise (S/N) is broadcast to the ground and if the S/N is high enough it is sent out to the community in a short, machine readable, GCN Notice. Robotic telescopes have been set up to read these Notices and slew to the location for early wide angle optical observations. The downlinked burst buffers are analyzed automatically by the ground software once they reach MIT. The *HETE* Science Team members review the automatic data and run additional analyses. For example, temperature data from sensors on the satellite can reduce the systematic error on the SXC location by allowing adjustment for thermal expansion. When the final ground analysis is complete, a GCN Circular is sent out reporting the updated position.

1.4 Optical Observing

All the data taken for this thesis were in the optical or near infra-red (NIR) bands. Ground based observations at the Magellan Observatory were made through internal Target of Opportunity (ToO) proposals for MIT allotted time. Observations at other ground based observatories were made through collaboration with interested observers. Hubble Space Telescope (*HST*) observations of GRB 020531 (Section 2.4) were acquired by the MIT *HETE* Science Team through Director's Discretionary time, owing to the rarity of localized Short GRBs (Section 1.1.6). Other *HST* observations used in this thesis were acquired through the Multimission Archive at Space

Telescope Science Institute (MAST). The observations were reduced with the IRAF[1] *noao.imred.ccdred* package, except for the archival *HST* images, which use the On The Fly Reprocessing (OTFR) available from MAST, and most photometric and spectral analyses were also performed in IRAF. Additional image and data manipulation, including image astrometry, was performed in the Interactive Data Language (IDL) programming environment, with extensive use of programs in the IDL Astrolib, http://idlastro.gsfc.nasa.gov, written by W. Landsman.

1.4.1 The Magellan Observatory

The Baade and Clay telescopes are a pair of 6.5 meter telescopes at Las Campanas Observatory built by the Magellan Project collaboration. Both telescopes have alt-azimuth, f/1.25 primaries and instruments at three or four f/11 Nasmyth focii. Push-pull actuators adjust the surface of the primary and the positions of the secondary mirrors every 30 seconds to compensate for thermal distortions and external forces on the telescope (Schechter et al., 2003). Combined with the stable atmospheric conditions in the Chilean Andes, very good seeing can be achieved, often less than an arcsecond. ToOs are reserved during MIT blocks of observing time at Magellan, and used to obtain both early and late time observations of *HETE* bursts, whenever possible. The majority of the observations in this thesis were made with either the Low Dispersion Survey Spectrograph (LDSS2) in imaging mode, or the Raymond and Beverly Sackler Magellan Instant Camera (MagIC). For the years 2001 and 2002, both of these instruments were on the Baade telescope, the first of the two Magellan Telescopes to be built. The Clay telescope began science operations during the summer of 2002, and both instruments were moved to Clay later that year.

The Low Dispersion Survey Spectrograph

The LDSS2 is designed as a multiple or long slit spectrograph, but can also be used to directly image the full 7.5′ diameter FOV reaching it (Figure 1-11). The outer arcminute of the field is somewhat distorted, but the inner 6.4′ is useful for fast, wide field searches. The plate scale of the SITe#1 2048×2048 CCD on the LDSS2 is 0.378 arcsec/pixel, which does not fully sample the point spread function of the 6.5 meter Baade and Clay telescopes, but does allow for fast exposures. The readout noise of the CCDs is 7 e^- rms and the gain is 2.2 e^-/ADU. Bias frames and dome flat fields are taken for each night of observation. Dome flats are taken by unfocused imaging of a quartz light shining on a region of the dome. Good flat fielding is essential for imaging with LDSS2, as the optics are rather dusty and the throughput changes significantly across the wide image. Both these issues are very apparent in Figure 1-11(a), a typical flat field. The final flat is created from a sigma-clipped average of multiple exposures. If multiple star fields have been imaged in a night, $\sim$ 10 non-matching star fields can be combined to create a "sky" flat. Sigma clipping will remove the stars, as long

[1]IRAF is distributed by the National Optical Astronomy Observatory, which is operated by the Association of Universities for Research in Astronomy, Inc., under cooperative agreement with the National Science Foundation.

as they do not overlap in the majority of images. If available, sky flats are often a better match to the dust spots and throughput of LDSS2 than the dome flats, as they sample the same night sky spectrum underlying the images.

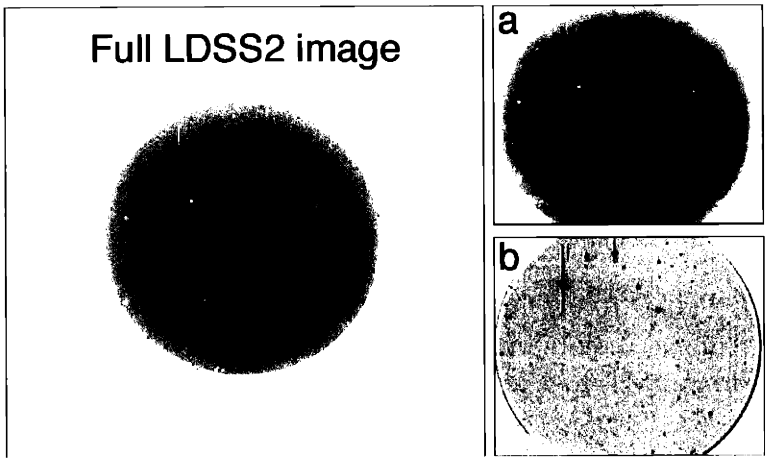

Figure 1-11 *Left Panel*: A raw exposure from LDSS2, showing the full 2048×2048 image. The 7.5′ FOV is imaged in the center, but most of the chip is left empty. *Right Panel*: (a) The central region of typical flat field image from LDSS2, showing dust spots and the reduction in throughput near the edge. (b) A final image, after bias subtraction and flat field division. Saturated pixels in bright stars have bled into the surrounding column pixels.

The Magellan Instant Camera

MagIC is the highest resolution optical imaging camera in use at Magellan, a SITe 2048×2048 CCD with a plate scale of 0.069″ per pixel for its 2.36′ square FOV. The zero point magnitude is 26.60 in R band for MagIC , and 26.76 in r'. The four quadrants of the chip are read out separately by four different amplifiers to speed up the readout time, each with their own overscan regions for additional bias calibration (Figure 1-12). The gain and noise for each amplifier differ slightly. The average gain is $\sim 2\ e^-$/ADU, and average readout noise is 5.3 e^- rms. A single frame is reassembled digitally by trimming the overscan regions and subtracting the average value of each from the respective quadrant. The same overscan process is run on each flat field and bias image taken. Usually bias images are taken each night, but the same flat fields can be used for consecutive nights. The filters and optics of Magic are currently very clean and dust spots are not a problem. Dark images are not used for MagIC as the dark current in the chip is generally smaller than the amplifier read noise. Unless the seeing is very good (> 0.5″), which can occur at the telescope site, the 0.069″ pixels usually over sample the telescope PSF, and binning images 2×2 is useful for faint sources. Cosmic ray rejection in the images is very simple when the PSF is so well sampled, however.

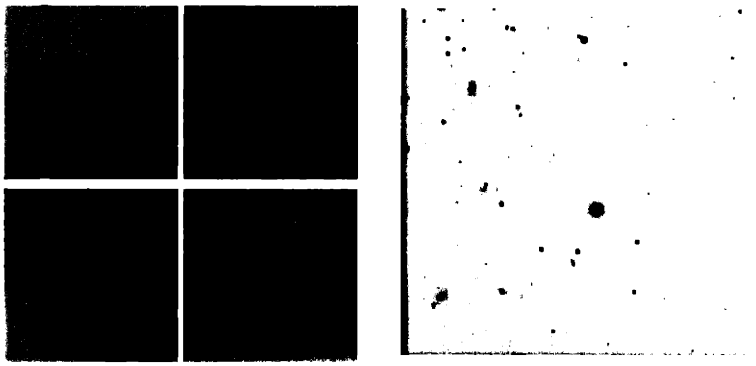

Figure 1-12 *Left Panel*: A raw image from MagIC showing the quadrants divided by their overscan regions, (colors inverted). *Right Panel*: The final image looks smooth after overscan subraction, bias subtraction, and flat field division.

IR Imaging with Classic Cam

Our IR observations of GRB 030115 (Section 2.5) were taken with the Classic Cam IR instrument on the Baade telescope. Classic Cam is a Rockwell NICMOS-3 HgCdTe array with a 256×256 array of 40 μm pixels. It was positioned at one of the f/11 foci of the 6.5m Baade telescope, but is no longer in use, having been replaced by a larger instrument. The Classic Cam imager had a maximum FOV of $29'' \times 29''$, which made accurate telescope pointing essential. We used the K-short filter which is centered at 2.16 microns with a bandwidth of 0.41 microns. The sky is quite bright in this band (120 ADU/sec per pixel) and short exposures (< 60 sec) are necessary to keep bright sources in the field from saturating. Each exposure is then dark corrected, with an average image constructed from $\sim$10 closed filter readouts, and flat fielded, with an average flat field image constructed from either images of a blank sky region, or the inside of the dome. Usually many ($\sim$50) images are taken for each field observed and summed to increase the S/N. Each set of four images are dithered, in a $\sim 5''$ square, to allow cleaning of hot pixels in the array, which reduces the fully imaged area to $20'' \times 20''$. The observer usually attempts to place at least one star, visible in the short exposures, in the FOV as a guide. The zero point magnitude for the Ks band is 22.8. The limiting magnitude for a 60 second exposure is about a magnitude deeper than the 2MASS catalog for K-short, but with the small FOV, few sources are visible in any field away from the plane of the Galaxy. For our observations of GRB 030115, only one guide star was visible in the 60 second exposures.

1.4.2 The Hubble Space Telescope

HST [2] observations were made by the MIT *HETE* Science Team for GRB 020531 (Section 2.4). We observed two of the Chandra X-ray Observatory (*CXO*) sources (Butler et al., 2003b) detected inside the *HETE* error box with the Space Telescope Imaging Spectrograph (STIS) (Bloom, Kulkarni & Djorgovski, 2002), a 1024 × 1024 SITe CCD, using the Clear filter mode. The CCD has a 52″ × 52″ field of view and ∼ 0.05″ pixels. The Clear filter has a central wavelength of 585 nm and a width of about 440 nm, which is similar to a R band in peak response but much wider, effectively equal to the detection efficiency of the CCD. The Clear filter is useful for imaging of faint sources in the shortest amount of time, as the limiting magnitude of STIS in Clear is about a magnitude deeper than any other instrument setup available at that time on *HST* . For GRB 020531, reduction was performed at STSci before we received the images. Publicly released Clear filtered STIS images were also retrieved and examined for GRB 020331 (Section 2.3), using the "on-the-fly" processing supplied by MAST (Section 1.4.3).

For GRB 030115 we retrieved archival *HST* Near Infrared Camera and Multi Object Spectrometer (NICMOS) and Advanced Camera for Surveys (ACS) images. The NICMOS (Dickinson et al., 2002) images were taken with Camera NIC3, the lowest resolution and highest sensitivity of the three 256 × 256 HgCdTe arrays used in the instrument, with a 51.2″ × 51.2″ FOV and 0.2″ pixels. The F160W filter, a very wide band filter centered at 1.6 microns and stretching from ∼1.1 to ∼1.9 microns, was used for the observations. This filter has a similar central wavelength to the H band NIR filter (1.65 microns) used at ground based observatories. The H filter has a width of only 0.3 microns, however, set by atmospheric absorption, so it is difficult to compare NICMOS photometry to ground based observations. NICMOS was run in MULTIACCUM mode during the observations, which breaks each observation into multiple exposures for use in cosmic-ray rejection. The ACS (Mack et al., 2003) observations of GRB 030115 were taken in Wide Field Channel (WFC) mode, giving a 202″ × 202″ FOV. The ACS WFC is a mosaic of two SITe 2048 × 4096 CCDs with ∼ 0.05″ pixels. Multiple filters can be used for imaging with ACS, including equivalent filters to the Sloan $griz$ and Johnson-Cousins BVI, as well as a wide band VR filter.

1.4.3 Using Archival Optical Data

When making early, wide field observations to search for GRB optical afteglows, often only one epoch of imaging is made. Comparisons with archival data are used to find any new sources which may be associated with the GRB. The Space Telescope Science Institute (STSci) maintains a digital archive of all sky surveys called the Digitized Sky Survey (DSS) with the full sky coverage in the R band. Most DSS plates reach to at least $R \sim 20.5$, if not slightly deeper, and this is the nominal

[2]Based on observations made with the NASA/ESA Hubble Space Telescope, obtained at the Space Telescope Science Institute, which is operated by the Association of Universities for Research in Astronomy, Inc., under NASA contract NAS5-26555.

limiting magnitude quoted when using the DSS as a template for new source searches. Deeper comparisons are not reliable, as noise fluctuations can simulate faint sources for poorly sampled PSFs. The Two Micron All Sky Survey (2MASS) is an all-sky survey conducted in the J, H, and Ks NIR bands and publicly available in digital form, http://pegasus.phast.umass.edu/. Both images and photometry tables have been posted. The limiting magnitudes for the J, H, and Ks bands are 15.8, 15.1, and 14.3, respectively.

MAST, http://archive.stsci.edu, contains an archive of all publicly available data taken by *HST* and many other image catalogs, including the DSS. Searches can be made for all *HST* imaging covering a specific position on the sky, and any public data, both raw and processed, may be retrieved. Most data taken by *HST* becomes public about three months after aquisition. OTFR (Lubow & Pollizzi, 1999) of *HST* NICMOS, STIS and ACS images has become the standard data product available publicly from STSci, although the raw data is also available for private processing. OTFR data uses the best currently available flat field, dark current, and bias images to correct the raw images requested. For ACS, if multiple exposures are available in a set, then cosmic-ray rejection is automatically performed, and then the final images are adjusted for the non-uniform plate scale of the instrument.

1.5 Thesis Overview

This focus of this thesis is the observation of GRB optical afterglows, with the goal of increasing knowledge of a sparsely sampled phenomenon. The few densely sampled optical afterglow lightcurves show almost as much variation as do their prompt, gamma-ray counterparts. As part of the *HETE* Science Team, I have led optical follow-up observations of multiple *HETE* GRBs, five of which are discussed in this thesis. In addition, I discuss a more complete analysis of two afterglows for which I aided in the original work, XRF 011212 (Section 2.2) and GRB 020331 (Section 2.3). As a graduate student at the MIT Center for Space Research (CSR) working in optical astronomy, I have been given access to the MIT shared time at the Magellan Observatory (Section 1.4.1) for thesis related observations. Usually one or two members of the CSR optical community travel to Chile to perform observations for the entire group, during each MIT time block. During August, 2002, I traveled to the Magellan Observatory to aid in observations, and was also able to take a spectrum of an optical candidate for GRB 020531 with LDSS2 while there (Section 2.4). The rest of the observations at the Magellan Observatory discussed in this thesis were made by other members of the CSR optical community, following the specifications of proposals I co-authored with other members of the MIT *HETE* Science Team. Collaborative observations of XRF 011212 at the University of Hawaii telescope, and GRB 020531 at the Subaru Telescope, both on Mauna Kea in Hawaii, were made for the MIT *HETE* Science Team. The results of my reduction and analysis of these observations are detailed in Table 2.1. I also analyzed the proprietary *HST* observations of GRB 020531 (Section 020531), made for the MIT *HETE* Science Team with Director's Discretionary time, after automatic reduction at the Space Telescope

Science Institute (STSci).

1.5.1 My role in the *HETE* Mission

For the past two years, I have also been working as part of the *HETE* Operations Team at MIT. As a duty scientist (DS), I have learned the operations of the complete satellite system, including the science instruments and software onboard the satellite (Seciton 1.3.1), the PGS systems, and the monitoring software on the ground. The satellite is monitored by one DS each week, and automatic responses by the ground software to potential GRB events, or problems with the system, are sent to a pager carried by the DS. *HETE* is termed a "walk-away safe" system because problems encountered by the system are often dealt with by automated software. DS intervention is only needed in extreme situations. The DS also acts as a filter for marginal detections of GRB-like events. If an event detected by the onboard software is not obviously a GRB, the DS will still be notified and must decide whether to initiate ground analysis.

Chapter 2

Observations of HETE GRB Afterglows

2.1 Introduction

Current GRB science relies heavily on the collaborative work of many astronomers around the globe making observations in many wavebands. Each location announcement of a GRB is followed by a race to find the afterglow (Section 1.2) and gain as much information as possible before the it fades away. Within this fast growing field, every burst is distinctive and has the real possibility of paving new ground. For this reason the GRB community uses the GCN, an online publication system based at the NASA Goddard Space Flight Center, to quickly disseminate relevant information on each GRB.

Our observations are listed in Table 2.1. Most of our observations were made at the Magellan Observatory (Section 1.4.1) during the MIT observing phases. We used either the wide field LDSS2 for early observations and afterglow searches, or the narrow field MagIC for late time photometry, when arcsecond afterglow positions were known. For XRF 011212 (Section 2.2) and GRB 020531 (Section 2.4), observations were made at Mauna Kea in collaboration with observers there and reduced at MIT. For GRB 020531 (Section 2.4) and XRF 030723 (Section 2.7) the MIT *HETE* Science group was able to make Chandra X-ray Observatory (*CXO*) observations in conjunction with early wide field optical observations. A combined search for new sources at both wavelengths was then undertaken, and in the case of XRF 030723, an afterglow candidate (Fox et al., 2003b), was confirmed to be fading in both our optical (Dullighan et al., 2003b) and X-ray observations (Butler et al., 2003d).

Table 2.1. Optical Observations and Photometry of Seven HETE GRB Afterglows

GRB	GCN[a]	t-t0 days	Filter[b]	Afterglow[c] Mag	Error	Telescope & Instrument	Exposure
20011212	1324	2.0	R	>24.5		6.5m Baade, MagIC	240 sec
"	1324	3.0	R	>24.5		6.5m Baade, MagIC	240 sec
"	1324	66.2	VR	>24.5		2.2m UofH	600 sec
20020331	1339	0.53	R	21.05	0.11	6.5m Baade, LDSS2	90 sec
"	1382	8.33	R	23.8	0.2	6.5m Baade, LDSS2	200 sec
"	1382	12.48	R	24.0	0.3	6.5m Baade MagIC	3x600 sec
20020531	1434	1.15	R	>23.6		6.5m Baade, LDSS2	180 sec
"	1434	5.41	R	>25.5		10m Subaru, SuprimeCam	420 sec
"	1434	10.11	R	>24.0		6.5m Baade, LDSS2	360 sec
20030115	–[d]	6.0	Ks	>22		6.5m Clay, ClassicCam	45x60 sec
20030418	2236	2.60	R	23.3	0.1	6.5m Clay, MagIC	3x300 sec
"	2236	2.61	I	23.0	0.1	6.5m Clay, MagIC	300 sec
"	2236	6.58	R	24.9	0.4	6.5m Clay, MagIC	2x400 sec
"	2236	6.59	I	>24.0		6.5m Clay, MagIC	400 sec
"	2236	6.60	V	25.1	0.5	6.5m Clay, MagIC	400 sec
20030723	2326	1.04	R	21.13	0.05	6.5m Clay, LDSS2	4x360 sec
"	2336	5.12	R	24.2	0.3	6.5m Clay, MagIC	3x200 sec
20030725	2384	6.81	r'	22.25	0.05	6.5m Clay, MagIC	2x300 sec
"	2384	7.68	r'	22.55	0.05	6.5m Clay, MagIC	2x360 sec

[a]Either the magnitude of the GRB afterglow measured in the observation, or the upperlimit if the afterglow was not detected.

[b]Harris V, R, Mould I, Sloan r'

[c]The GCN Notice in which we published each observation is noted.

[d]Not published in the GCN, Dullighan et al. (2004)

2.2 XRF 011212

2.2.1 The *HETE/RXTE* Localization of XRF 011212

GRB 011212 (=U10827) (Ricker et al., 2001) was detected by *HETE* (Section 1.3) on December 12, 2001 at 04:04:02 UT. The burst did not trigger on board the satellite, but was found by automatic ground analysis of WXM survey data. A location was reported to the GCN at 12:24:04 UT. The Rossi X-ray Timing Explorer (*RXTE*) All Sky Monitor also observed this burst during its routine all-sky survey, and a combined error box was sent through the GCN at 18:48:53 UT. Follow up observations began soon after the reports were distributed (Fox et al., 2001a), but because of the delay between the burst and ground trigger, this was not soon enough to discover an optical transient.

Classified as an XRF (Section 1.1.4), this burst was very soft and did not have enough hard photons to trigger in Fregate. Triggering on WXM data on board the satellite was not regularly used when GRB 011212 occurred, as the highly variable background was not yet well understood. False triggers on high energy particles and known Galactic sources could not be easily discerned from real events by the original triggering software onboard the satellite. New algorithms cross-referencing position data with the WXM lightcurve triggering were under testing during 2001, and are currently working well for on board triggering of XRFs (eg, XRF 030723, Section 2.7). The burst also occurred before the HETE Science team had a standardized way of reporting untriggered events. XRF 011212 is now recorded with the Untriggered Burst ID (UBID) 10827 in the official *HETE* untriggered burst catalog, not H10001 as initially reported to the GCN (Ricker et al., 2001).

2.2.2 Optical Observations

We made three epochs of observations to search for fading sources in the the *HETE* / *RXTE* error region for GRB 011212 at 2.0, 3.0, and 67 days after the burst (Dullighan et al., 2002a, Table 2.1). The first two epochs covered the full error box with a 12 field mosaic of MagIC at Magellan (Section 1.4.1), and the last was a three field mosaic taken with the 2.2 meter University of Hawaii telescope on Mauna Kea. All three epochs had a limiting R band magnitude of 24.5, except for the last few frames of the second epoch. The seeing for the first epoch was steady at $0.7''$ through the first night and most of the second, and then degraded to $1.3''$ as our observations were finishing on the second night. The images from the University of Hawaii telescope were taken for us by D. Tholen over two nights, February 16.33 and February 17.38 UT with seeing on both nights of $1.3''$. We treat them as a single epoch, however, as most GRB optical afterglows would be below our detection limits by $\sim$60 days.

A search for fading sources was made between the epochs of imaging, first by visually comparing the matching fields from the first two epochs. We then used the IDL Astrolib function *find* to systematically search for all sources above the limiting magnitude of the first epoch. Relative astrometry was measured between the epochs and the photometry was performed at the positions of all the sources found in the

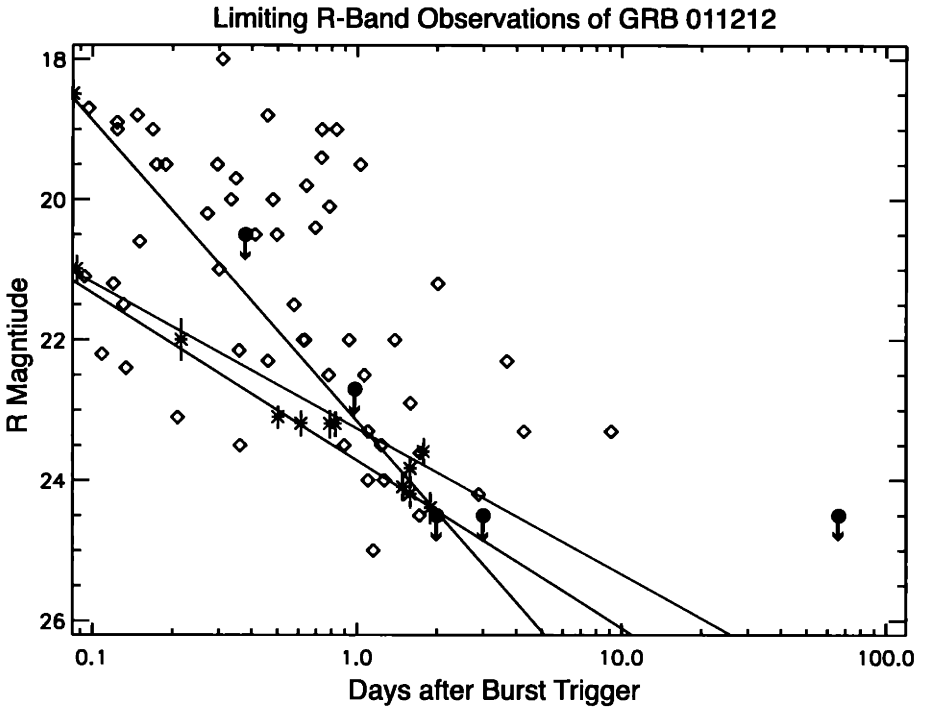

Figure 2-1 This plot compares the most limiting R magnitude upper limits (filled circles) measured for XRF 011212 (Kinugasa et al., 2001; Saracco et al., 2001; Dullighan et al., 2002a) to the most limiting measurements for each observed, but undetected, Long GRBs since 2000 (diamonds, data from the GCN). Also plotted are the R band data and fit decay slopes for the afterglows of 3 faint GRBs; red, GRB 030227 (Castro-Tirado et al., 2003a); green, GRB 021211 (Kinugasa et al., 2002; McLeod et al., 2002; Levan et al., 2002); blue, GRB 020124 (Berger et al., 2002; Gorosabel, 2002; Torii et al., 2002).

first epoch. The only sources found to fade were very close to the limiting magnitude in the first epoch, so their significance is not high.

2.2.3 Conclusions for XRF 011212

No definitive fading sources were seen between the three epochs of imaging. Figure 2-1 shows our upperlimits compared to the most limiting R band or unfiltered CCD observations for all observed but undetected Long GRBs reported to the GCN since 2000. Observations which did not reach deeper than a previous observation of the same burst were excluded for clarity. We used the compilations of optical observations on the GRBlog webpage (Quimby, McMahon, & Murphy, 2003) for each burst. The early observations of XRF 011212 reach an average limit, compared to the other limiting observations, and our late time observations are deeper than most.

Our upper limits on the magnitude of its afterglow places XRF 011212 in at least the very faint, or fast fading category, if not in the "Optically Dark" GRB

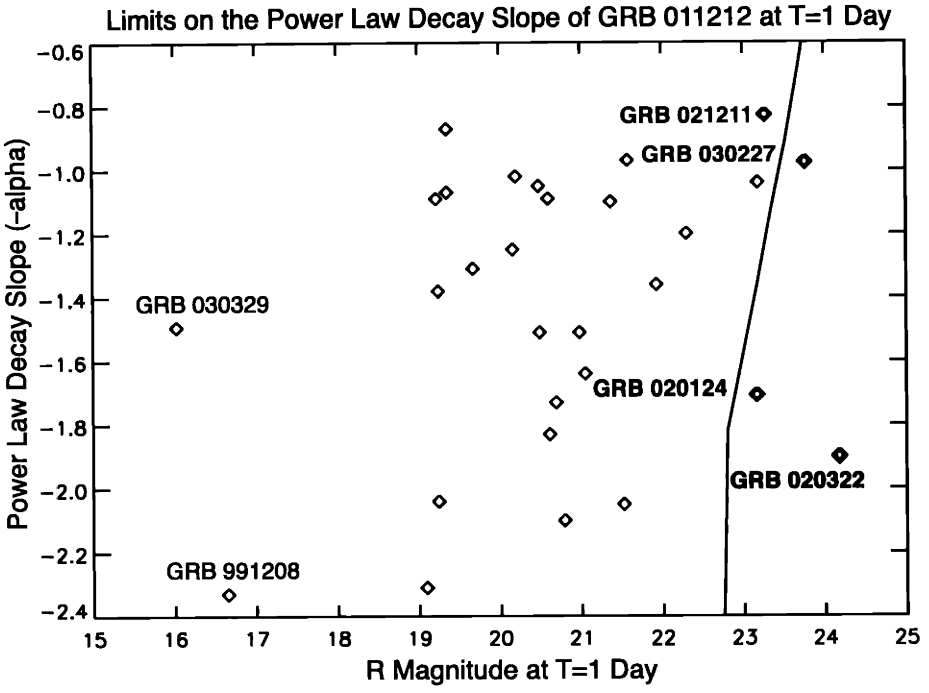

Figure 2-2 The shaded area describes the region of undetectable afterglows as limited by our observations of XRF 011212 and the data from the GCN (Kinugasa et al., 2001; Saracco et al., 2001), as shown in Figure 2-1. All GRB Afterglows with at least 3 optical measurements between 0.1 and 10 days as reported to the GCN, have been fit with a simple $F = F_0 t^{-\alpha}$ decay. Most optical afterglows are found on or about 1 day when reasonably deep optical searches ($R \sim 24$) are performed.

category. There are only three out of ~ 30 currently detected GRB afterglows below our sensitivity threshold. This threshold is a combination of the non-detection by early observers reporting to the GCN (Kinugasa et al., 2001), and a non-detection in our deep late time observations of the burst. We assume that for early searches where images are compared to the DSS (Section 1.4.3) any new source 0.3 magnitudes above the limit of the DSS would be reported. For our searches we define the threshold for a fading source as 0.3 magnitudes above the limit in the first epoch and at least 0.5 magnitudes fainter in the next. The grey region in Figure 2-2 shows the parameter space for fading sources below the detection limit, normalized to one day after the trigger time. Faint, fast fading afterglows ($\alpha > 1.5$) such as that seen for GRB 020124, would not have been detectable for this burst because of the initial delay of ~ 8 hours before localization, but our late observations place reasonably deep limits on any slower fade.

2.3 GRB 020331, The Easter Burst

GRB 020331 (=H1963) (Ricker et al., 2002a) was detected on March 31, 2002 at 16:32:28.76 UT onboard the satellite by the FREGATE and WXM. An alert was sent to the GCN within seconds, and the initial WXM location was distributed about 40 minutes later. The final ground analysis produced an error circle with an 8′ radius centered at RA = 13h 16m 22.7s, Dec = -17° 55′ 23″ (J2000) (Ricker et al., 2002a). This was a classic "Long" GRB, having a T_{90} of 56 seconds and an E_{peak} of 129 keV.

2.3.1 Optical Observations with Magellan

Three observations of the field of GRB 020331 were made at the Magellan Observatory (Section 1.4.1). The first two were taken with the LDSS2 camera in imaging mode. The first set of observations were taken only 12.7 hours after the burst and before the identification of the optical counterpart of the burst. A mosaic of seven 90 second R band images were used to cover the entire WXM error circle, reaching a limiting magnitude of R$\sim$23.5 and the images were compared to the Digital Sky Survey by eye, to search for new sources. No obvious new sources were found and a follow up observation with LDSS2 was scheduled. Before the second observations took place, an Optical Transient (OT) was reported to the GCN by Fox et al. (2001b), measured at R$\sim$21 in observations 17 hours after the burst. We reviewed our observations and found the source reported at R =21.05 $\pm$ 0.11 magnitudes (Dullighan et al., 2002b).

Later observations were taken after the report of the OT, at 8.33 days and 12.48 after the burst, and so could be limited to the field surrounding the OT. Two 200 second R band images were taken of the field at 8.33 days using the LDSS2 instrument, and reached a limiting magnitude of $R \sim 24$. The OT was measured at $R = 23.1 \pm 0.2$, confirming the fading nature of the OT. We calculated a decay rate of $\alpha = 0.62$ between our observation and reported the fade to the GCN (Dullighan et al., 2002c).

The third set of observations were taken with the MagIC instrument on Magellan, which has much higher resolution. One 300 second and three 600 second R band images were combined to reach a limiting magnitude of $R \sim 24.5$. The third observations showed the OT to have only faded to $R = 23.2 \pm 0.3$, and the higher resolution images showed the source to be extended, with the centroid 0.8" to the East of the original OT position, as shown in Figure 2-3. This suggested to us that we were now observing an underlying galaxy, and not the OT. Subtracting a point source Point Spread Function (PSF), created from a combination of stars in the field, from the new centroid of the OT left a residual at the original OT position (Dullighan et al., 2002d). This source to the East was confirmed to be a galaxy by late time high resolution *HST* STIS images, as reported by Soderberg et al. (2002a). In the *HST* images this galaxy is separated from the point source OT (Figure 2-4). It is not clear whether this galaxy is associated with the host of the GRB, as no redshift is available for either object.

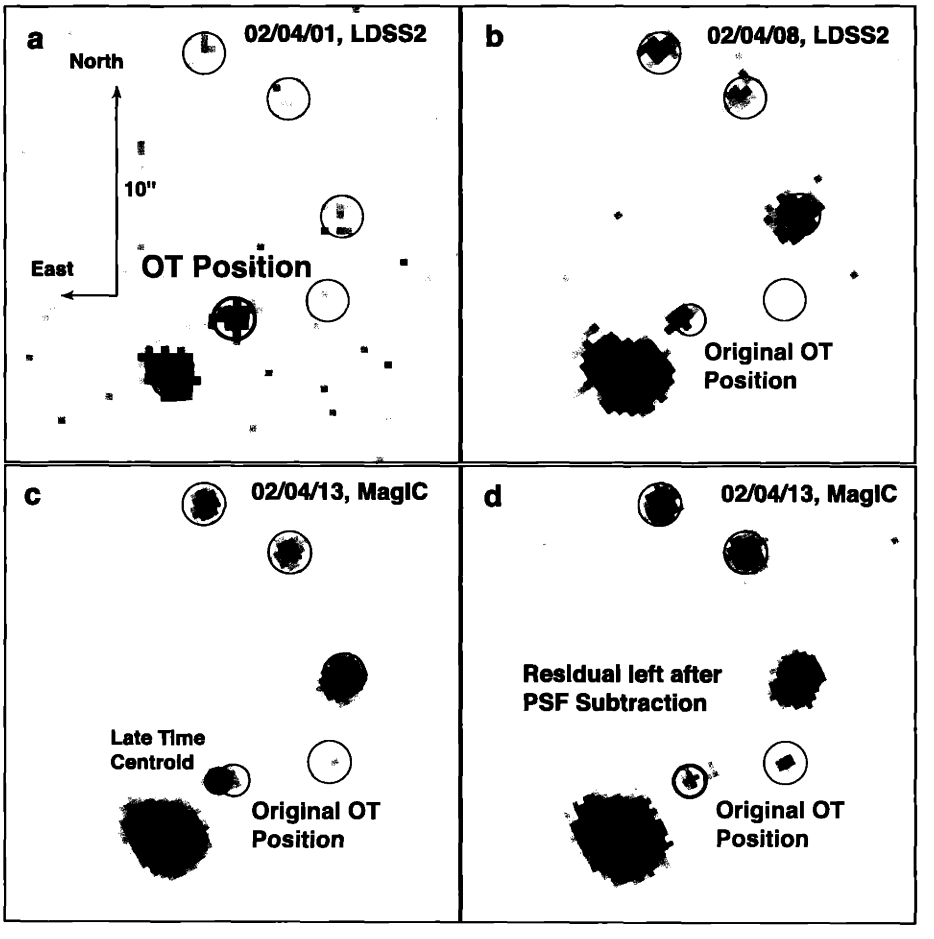

Figure 2-3 Images of the afterglow of GRB 020331. a) and b) are the first and second epochs of LDSS2 imaging, respectively. The OT centroid seems to shift between these two observations. The third epoch image from Magic is image c), and d) is the same, but with an R =23.6 magnitude point source PSF subtracted from the late time OT centroid. A residual of R =24 is left at the position of the original bright OT. The red circle is at the original OT position in all images and the green circles are comparison sources used to match the astrometry. The blue circle marks the shifted late time source centroid.

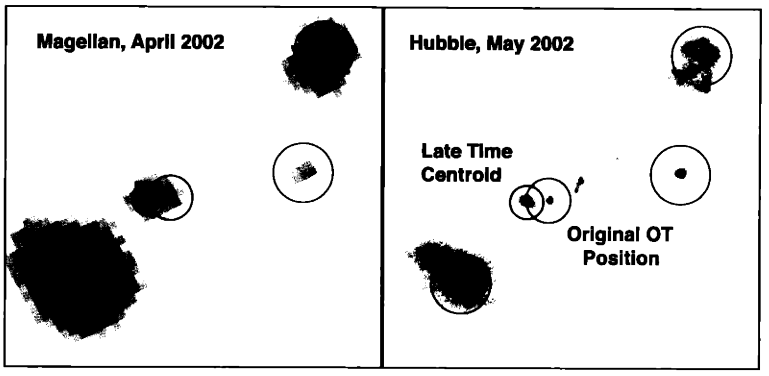

Figure 2-4 The late time afterglow of GRB 020331. A comparison between the MagIC image from April 13, 2002 and an image from archival *HST* STIS images taken in May of 2002. Our late time centroid for the OT matches that of the galaxy to the East in the *HST* image. We aligned our astrometry using field stars and marked the same positions as in Figure 2-3.

2.3.2 Discussion

The *HST* four epochs of STIS Clear imaging taken in April and May of 2002 (Soderberg et al., 2002a), became public later that year and we retrieved them for comparison with our own data. We also retrieved the final epoch of imaging taken of GRB 020331 with the same instrument setup on August 18, 2002. All five epochs of STIS imaging of GRB 020331 were taken as part of the Cycle 10 *HST* observing program #9180. Using the automatic reduction provided by the MAST archive (Section 1.4.3), we stacked the multiple images available in each epoch for cosmic ray removal and performed aperture photometry on the sources in each epoch. The magnitude of the OT on August 18, 139.6 days after the burst, was measured as $R = 25.2 \pm 0.1$ mag, using relative photometry from the other four epochs to fit to the magnitudes reported for the OT by Soderberg et al. (2002a). We also measured the magnitude of the galaxy to the East as $R = 23.9 \pm 0.1$, which did not vary between the five epochs. In order to simulate the equivalent photometry from the ground, we added the magnitude of this galaxy to the magnitude of the OT in the first three *HST* epochs. The lightcurve of the afterglow was then fit to a power law fade plus a constant source, with $F = F_0 t^{-\alpha} + F_{const}$ and $R = R_0 - 2.5log(F)$, where F_0 and R_0 are scale factors fit to the data. Using our Magellan data and earlier data points from the GCN (Price et al., 2002; Kato et al., 2002), the best fit was obtained with $\alpha = -0.97 \pm 0.02$ and a constant magnitude of $R = 23.75 \pm 0.05$. The last two epochs of *HST* data were not used for this fit because a re-brightening of the afterglow is seen in this data. Subtracting the $R = 23.9$ eastern galaxy from the data gives a power law fit with a remaining constant source of $R = 26.0 \pm 0.1$ magnitude, which we assume to be the underlying host of the OT. Given this host galaxy magnitude, we measure the fade between the last two *HST* measurements as $\alpha \sim 0.65$, which is not as steep as before the rebrightening.

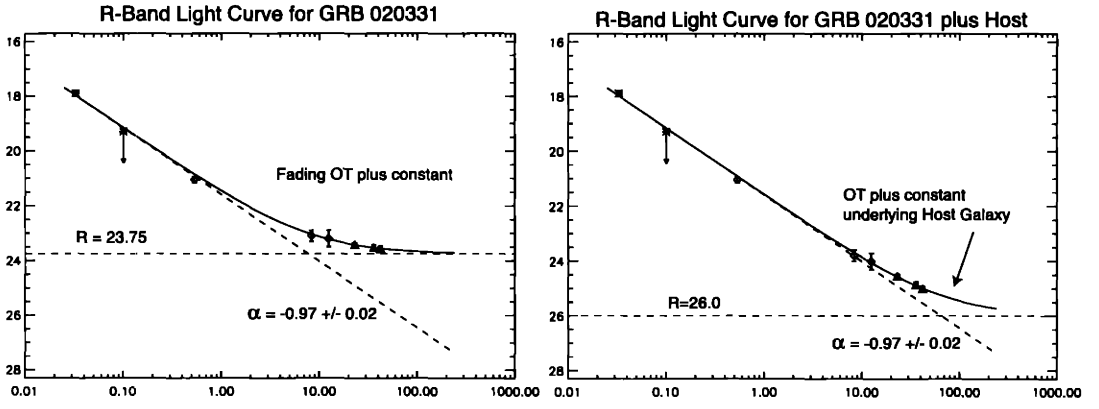

Figure 2-5 *Left panel*: The lightcurve for the optical afterglow of GRB 020331 with the R =23.9 source added to the first three *HST* OT magnitudes. The lightcurve is fit to a power law fade plus a constant source of R =23.75. *Right panel*: After subtracting R =23.9 from the Magellan OT magnitudes, a fit of a power law plus a constant at R =26.0 $\pm$ 0.1 is made with the original *HST* data. The stars are the GCN data (Price et al., 2002; Kato et al., 2002), the diamonds are our Magellan data, and the triangles are the data from the archival *HST* images.

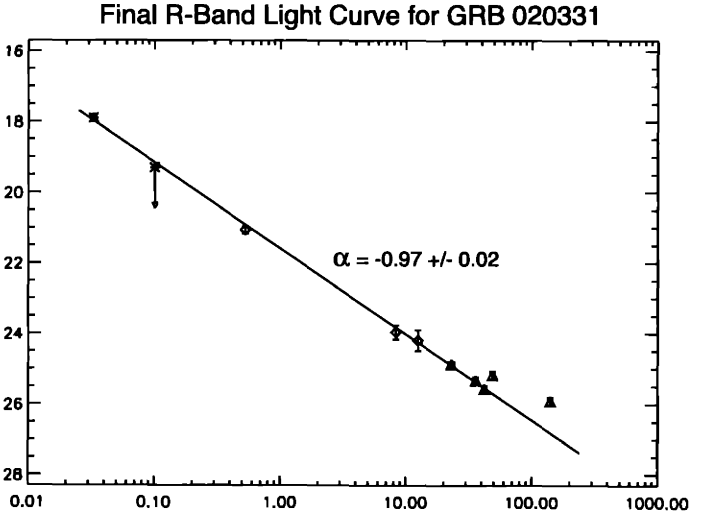

Figure 2-6 The final lightcurve for the optical afterglow of GRB 020331 after subtraction of the underlying host galaxy light and the contaminating galaxy to the east. The two final *HST* epochs show a rebrightening of the OT (Soderberg et al., 2002a). The stars are the GCN data (Price et al., 2002; Kato et al., 2002), the diamonds are our Magellan data, and the triangles are the data from the archival *HST* images.

2.3.3 Conclusions for GRB 020331

In conclusion, the host galaxy of GRB 020331 has not been observed to date, although we have determined its likely magnitude, at $R = 26.0 \pm 0.1$ mag, by measuring the flattening of the afterglow decay curve. This galaxy must be very small, as the source at the GRB position is only slightly larger than a point source in the *HST* observations. The decay of the afterglow is flat at α=-0.97 from about 0.03 to 40 days after the burst, showing no signs of a jet break. A rebrightening was seen by Soderberg et al. (2002a) at late times, rising between the *HST* STIS observations at 42.7 and 49.3 days after the burst. This excess is still evident in the STIS image at 139.6 days after the burst, with a shallow fade of $\alpha \sim 0.65$ between the last two points.

2.4 The Short/Hard GRB 020531

2.4.1 The Localization of GRB 020531

On May 31, 2002, at 00:26:18.73 UT, the *HETE* detected GRB 020531 (=H2024) (Ricker et al., 2002b) in both of the Fregate and WXM instruments. This GRB was classified as 'Short' (Section 1.1.6), having a T_{90}= 1.15s (7-400 keV) (Barraud et al., 2003). It was also a relatively hard burst, with E_{peak}= 729 keV and a flux ratio of 0.10 between the 7-30 keV and 30-400 keV bands (Barraud et al., 2003). The WXM instrument was able to localize the burst and sent down a position in spacecraft coordinates, as the real-time aspect of the satellite was not available onboard.

A preliminary localization was reported to the GCN at 88 minutes after the burst. Ground analysis produced a 90% confidence rectangle which was 43 arcminutes by 67 arcminutes, and was sent to the GCN ~5 hours after the burst (Ricker et al., 2002b). The addition of IPN data narrowed the box, initially to a $42' \times 42'$ box at 18 hours (Hurley et al., 2002b), and then to a polygon covering 22 square arcminutes ("IPN Region I") 5 days later (Hurley et al., 2002c). A final IPN/*HETE* error box was published 56 days after the burst that restricted the box to a diamond shaped region of 9 square arcminutes ("IPN Region II") (Hurley et al., 2002d).

Early observations were made possible by the *HETE* Team's prompt GCN announcement. Small robotic telescopes were able to begin observing just 90 minutes after the end of the burst (Castro-Tirado et al., 2002b) and place upper limits on the early time optical afterglows of this burst. Much deeper observations continued to constrain the optical afterglow in the following days and weeks, including the optical and X-ray observation performed by our group.

2.4.2 Optical Observations

On June 1.16 UT, 2002, 27.4 hours after the burst, seven 180 second LDSS2 (Section 1.4.1) images were taken to mosaic an early large *HETE* /IPN error box (Hurley, K., private communication). This first set of images was compared with the Digital Sky Survey to look for new sources that might be associated with the burst. All observations were made in the broad band Harris R filter. Our images had a limiting magnitude of R ~23.6, well below that of the DSS images used for initial comparison. Another set of 360 second LDSS2 images, with the same instrument setup, were taken on June 10.13 UT, 10 days after the burst. These images had a limiting R magnitude of ~24.0. By then, the IPN Region I had been published and only two fields were needed to cover the full error box.

The LDSS2 was also used in spectroscopic mode on August 10.01 UT, 2002, to observe the R ~20.5 magnitude optical counterpart of the X-ray source CXOU J151515.3-192511, Source 00 (Butler et al., 2002a), discovered inside the refined IPN Region II Chandra X-ray Observatory. A 300 second exposure was taken using the Medium-Blue grism with a 1.0 arcsecond slit.

Additional comparison images were taken at the National Astronomical Observatory of Japan (NAOJ) 8.2 meter Subaru Telescope on Mauna Kea in Hawaii on June

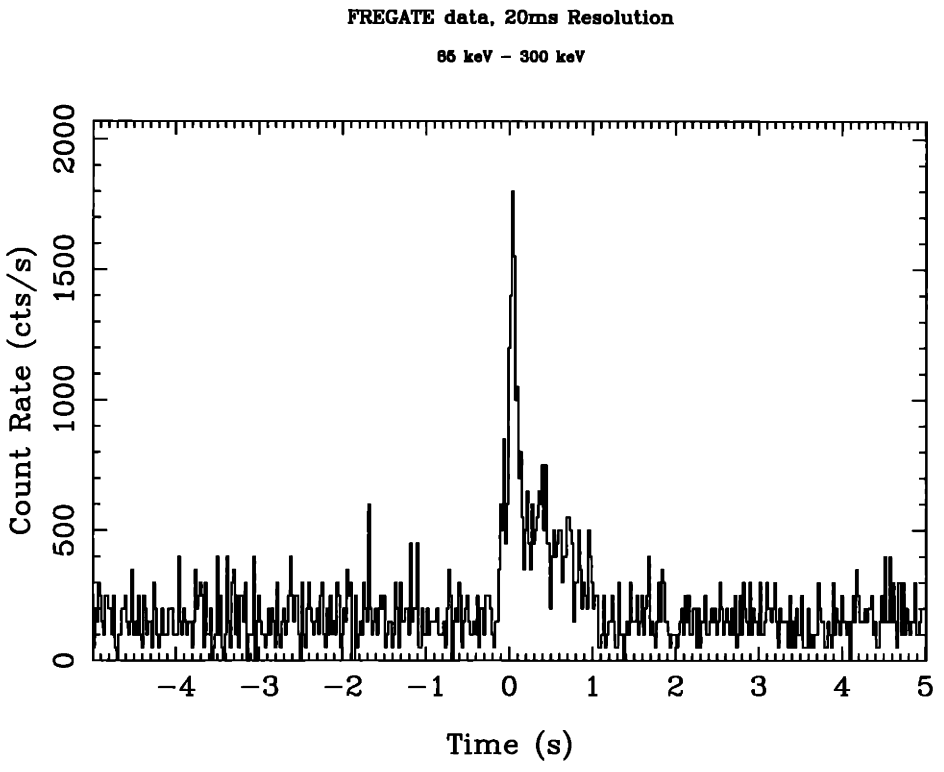

Figure 2-7 The FREGATE 20ms lightcurve for GRB 020531. The burst had a T_{90} of $\sim$1 sec and T_{50} of 360 ms.

5.43 UT. We were able to use the f/2 prime focus camera, Suprime-Cam (Miyazaki et al., 2002), which has a $34' \times 27'$ field of view. This allowed the entire IPN Region I to be imaged at once. Suprime-Cam is an imaging CCD mosaic of ten MIT/LL 2048×4096 CCDs with a plate scale of 0.20 arcsec/pixel. The readout noise of the CCDs is 10 e^- rms and the gain is 2.5 e^-/ADU (Miyazaki et al., 2002). Due to the $\sim$16 arcsecond gaps between the chips, three slightly offset images of 420 seconds each were taken to completely cover the field. Each set of images reached a limiting R magnitude of $\sim$25.5. Routine flat field and bias images were taken by the observers at Subaru and were downloaded in compressed form from Hawaii with the three sets of data images. We reduced the data in IRAF with the standard CCD reduction package, *ccdred*.

Late time observations were made with *HST* (Section 1.4.2), through proposal #9276, to determine the nature of the optical counterparts of two of the *CXO* X-ray sources which were found to have faded. The first observation was made of *CXO* Source 05 with STIS, in imaging mode, starting on 2002 June 13.187 UT with the Clear Filter. The second observation was of *CXO* Source 48 with the same configuration, and started on 2002 June 20.399 UT.

Table 2.2. X-Ray Sources of Interest for GRB 020531 (Butler et al., 2002a)

#	Chandra Name	RA h m s	Dec ° ′ ″	ΔRA(s)	ΔDec(″)	Counts[a]	Counts[b c]
	Inside Error Box[d]						
48	CXOU J151455.8-192454	15 14 55.76	-19 24 54.02	0.020	1.36	8	0
51	CXOU J151513.3-192450	15 15 13.30	-19 24 49.94	0.019	1.36	7	7
56	CXOU J151514.1-192428	15 15 14.14	-19 24 27.58	0.022	1.37	7	1
58	CXOU J151508.0-192338	15 15 07.96	-19 23 37.69	0.021	1.36	6	2
	Outside Error Box[d]						
00	CXOU J151515.3-192511	15 15 15.31	-19 25 10.71	0.019	1.35	70	22
05	CXOU J151517.8-192102	15 15 17.80	-19 21 02.20	0.020	1.36	45	15
15	CXOU J151458.3-192322	15 14 58.34	-19 23 22.32	0.020	1.35	20	8

[a]Epoch 1: 20 kiloseconds; 2002 June 5 04:00 - 10:04 UT (Butler et al., 2002a)

[b]Epoch 2: 10 kiloseconds; 2002 June 10 20:59 UT - June 11 00:13 UT (Butler et al., 2002b)

[c]The exposure for the Epoch 2 observations was half that of Epoch 1, so the Epoch 2 counts should be doubled before comparison.

[d]The 22 arcmin^2 error box reported by Hurley et al. (2002b)

2.4.3 The Search for Fading Sources

Astrometric and R band photometric calibrations were made using the calibration data reported by Henden (2002) for all three epochs of imaging. Aperture photometry was performed, using IRAF *apphot*, on all sources in the error box down to the limiting magnitudes of each image (Table 2.1). We constructed the source lists using an automated script written in IDL, based on the IDL Astrolib function *find*, to search for gaussian shaped sources. The source lists for each epoch of imaging were matched and the R magnitudes compared. No significantly fading optical sources were found inside the final IPN Region II.

2.4.4 Observations with *CXO*

Two epochs of observations were made of GRB 020531 with the *CXO* (Weisskopf et al., 2002) using the *HETE* science team Target of Opportunity time. The first epoch consisted of a 20 kilosecond imaging exposure with the ACIS-I array on June 5 from ~4 to ~10 UT, 5.15 days after the burst (Butler et al., 2002a). The $18' \times 18'$ field of view of ACIS covered the entire IPN Region I. The second epoch was a 10 kilosecond exposure of the same field with the same instrument setup, on June 10 from ~21 to ~24 UT, to look for fading sources (Butler et al., 2002b).

The first epoch observation found ten (0.5-8 keV band) sources inside the 22 arcmin^2 box. Three bright sources just outside the error box were also reported

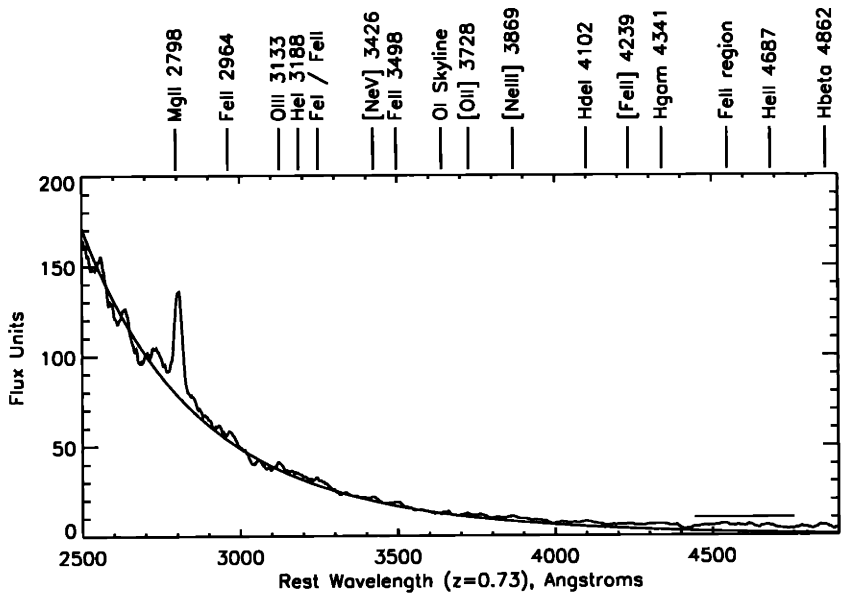

Figure 2-8 The optical spectrum of *CXO* Source 00, plotted in the rest frame of the Mg II emission line. A power law curve has been fit to the spectrum, which has been left in instrument flux units. Also marked are emission lines with average flux ratios greater than 0.150 compared to the average quasar Lyman α emission line (Vanden Berk et al., 2001).

(Butler et al., 2002a) (see Table 2.2 for a listing of the *CXO* Sources discussed). Many of these sources had optical counterparts in the Magellan images taken on June 1, including all three of the bright sources.

The second epoch observation to look for fading sources found that only two of the original ten sources inside the error box had faded with any significance (Sources 48 and 56). Two of the three bright sources also had faded (Sources 00 and 05). Only Source 48, however, had faded steeply enough to be consistent with a typical GRB power law decay of $t^{-1.3}$ (Butler et al., 2002b). Source 00 was also reported in the GCN circular as having faded, but with the specification that it had not faded steeply enough (Butler et al., 2002b).

2.4.5 Reports on Individual *CXO* Sources

Chandra X-ray Observatory Source 00

The brightest source found in the *CXO* observations, CXOU J151515.3-192511 (Source 00), faded significantly between the two epochs. In the first epoch ~70 counts were detected in 20 ksec, and in the second only 22 counts were detected in 10 ksec. This was well outside of its error range, giving a 0.03% likelihood of a chance fade due to poisson statistics. Source 00 is just inside the South-East corner of the final *HETE* /IPN error box (Hurley et al., 2002d). While its fade is significant, it is not steep enough to make Source 00 a likely candidate for the X-ray afterglow of GRB

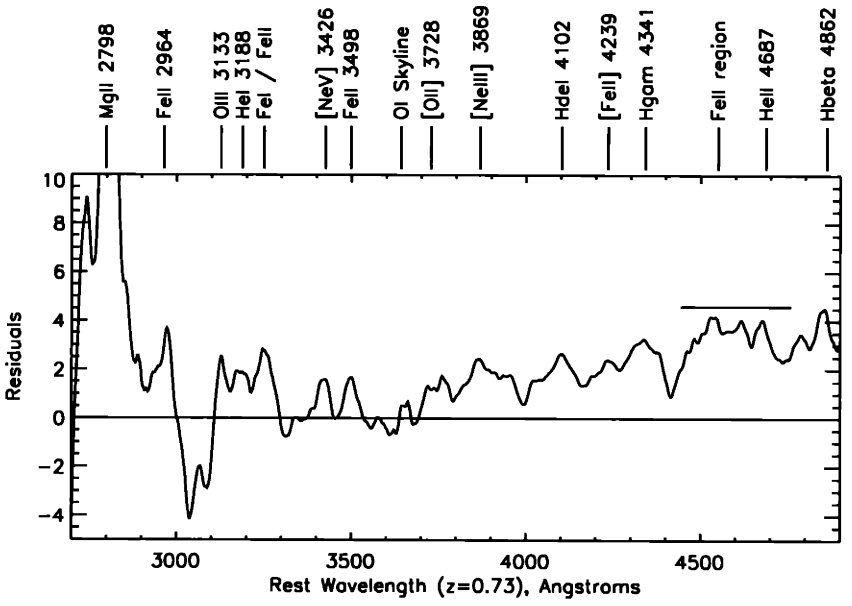

Figure 2-9 The residuals left after the subtraction of the power law fit. The vertical axis has been expanded to emphasize the low significance lines redward of the Mg II emission line. The O I skyline is marked at the position of the residual positive and negative flux left after the spectral background subtraction.

020531. The average X-ray afterglow fades at a powerlaw rate similar to the optical, having decay slopes with α of $\sim$1 or 2. This requires a fade of at least 2 to be within the range of believable afterglows.

CXO Source 00 had an optical counterpart in all three nights of ground based optical imaging, at R$\sim$20.5 magnitudes. The counterpart increased in brightness by 0.06 ± 0.03 magnitudes between June 5.43 and June 10.13 UT, but otherwise stayed relatively steady. This source is just visible at the limiting magnitude of the Digital Sky Survey image of the field, consistent with its magnitude after the burst, and implying that this is not a new source. A spectrum of the optical counterpart of Source 00 was taken on 2002 August 10.01 UT with the LDSS2 on the Magellan Baade 6.5m telescope. The spectrum indicates that this source is a quasar at z=0.73. The only strong feature in the spectrum, a line at 4840$\AA$, is identified as a Mg II line at a rest wavelength of 2798$\AA$ (see Figure 2-8). The continuum also matches the shape of such a redshifted quasar, decreasing sharply towards the red as a powerlaw. Broad Hydrogen β, γ, and δ Balmer lines at $\sim$8411$\AA$, $\sim$7508$\AA$, and $\sim$7094$\AA$, consistent with the z=0.73 redshift, (4862$\AA$, 4340$\AA$, and 4101$\AA$ respectively, in the rest frame) are measured at low significance (see Figure 2-9). Associated quasar metal lines at low significance are also consistent with this redshift.

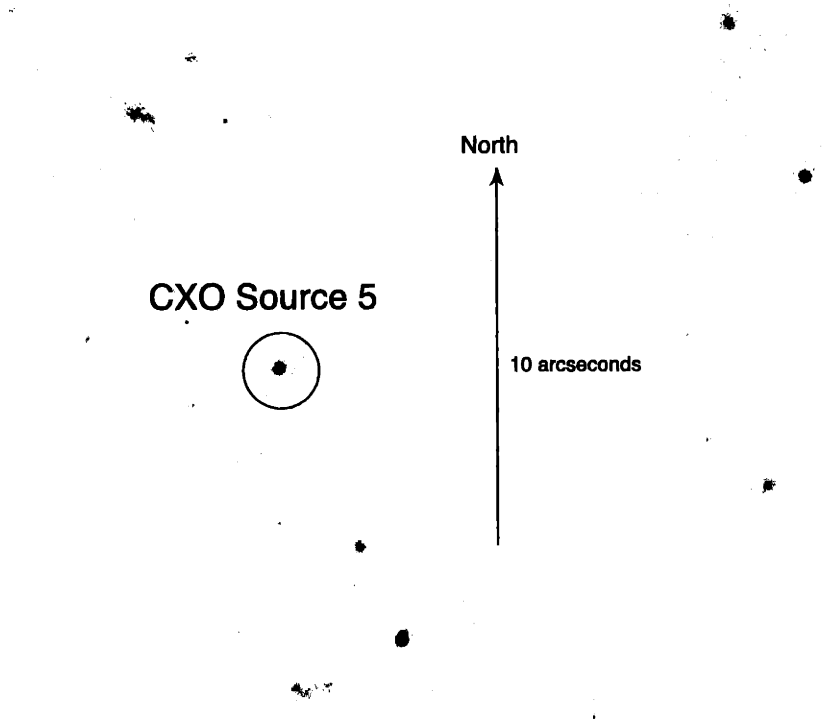

Figure 2-10 A portion of the *HST* STIS image of *CXO* Source 05. The circle has a 1" radius, and North is up with East to the left.

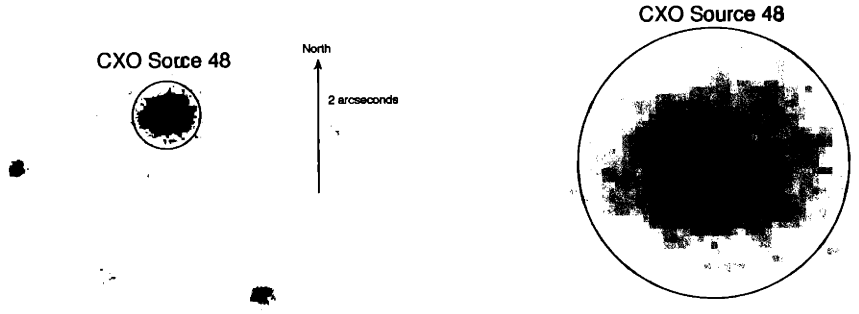

Figure 2-11 *Right panel*: A portion of the *HST* STIS image of *CXO* Source 48. *Right panel*: A zoomed and rescaled version to show the central structure of the galaxy. The circle has a 1" radius in both images. North is up and East is to the left.

Chandra X-ray Observatory Source 05

CXOU J151517.8-192102 (Source 05) was also a relatively bright point source in the X-ray images of the field of GRB 020531 (Butler et al., 2003b). It was positioned just outside the North East corner of the 22 square arcmin, *HETE* /IPN error box (Hurley et al., 2002c), but was much further outside the final 9 square arcminute box (Hurley et al., 2002d). The source was measured as a point source in all three epochs of optical imaging, June 1, 5, and 10 , 2002, originally at about R =23.1 $\pm$ 0.2 mag. The X-ray flux was steady to within error, but Source 05 caught our attention when the optical counterpart faded to R =23.79 $\pm$ 0.06 in the second epoch, and then faded additionally to R =24.0 $\pm$ 0.2 mag in the third epoch, as reported in GCN 1434 (Dullighan et al., 2002e). This is consistent with a decay index of alpha=0.35 $\pm$ 0.05, and also consistent, within error, with the slight fade in X-ray counts between the two *CXO* observations. An *HST* follow-up observation on June 13, 2002, however, showed a point source with no change in magnitude. The slope of the fade was also very shallow compared to that of the typical GRB afterglow, therefore it is likely that this source has nothing to do with GRB 020531.

Chandra X-ray Observatory Source 48

CXOU J151455.8-192454 (Source 48) (Butler et al., 2002a) was one of the few faint X-ray sources inside the 22 arcmin^2 error box (Hurley et al., 2002c). It was, however, outside the final 9 arcmin^2 error box (Hurley et al., 2002d). Source 48 faded significantly in X-rays, from 8 counts in the first epoch of measurements down to the background level in the second epoch (Butler et al., 2003b). This was the strongest fade of any of the X-ray sources in the field of GRB 020531. The optical counterpart was determined to be a small galaxy at a magnitude of R = 22.7 $\pm$ 0.1 mag, from the images taken with the Suprime-Cam (Miyazaki et al., 2002) on the Subaru telescope. No change in magnitude was seen between the three epochs of optical imaging. A spectrum of the galaxy taken with Keck II was reported by Kulkarni et al. (2002) placing the redshift of the galaxy at z=1.00. An *HST* image of the source was taken on June 20, 2002 resolved the internal structure of the galaxy in much greater detail, but no distinct point sources were found. Unfortunately, when the final *HETE* /IPN error box (Hurley et al., 2002d) was published, Source 48 was well outside the western edge of the box. It is likely that the X-ray source in this galaxy is an active galactic nucleus, and not associated with GRB 020531 at all.

Chandra X-ray Observatory Sources 51, 56, 58

The *CXO* Sources 51, 56, and 58 (see Table 1) were the remaining faint X-ray sources in the final *HETE* /IPN error box (Hurley et al., 2002d) for GRB 020531. Optical counterparts were found for Sources 56, at R = 20.5 $\pm$ 0.05 mag, and 58, at R = 23.9 $\pm$ 0.1 mag in our images. No optical counterpart was seen inside the 1" error circle of Source 51, down to the limiting magnitudes of all three epochs of imaging. None of these sources were seen to change in flux significantly in X-ray (Butler et al., 2003b)

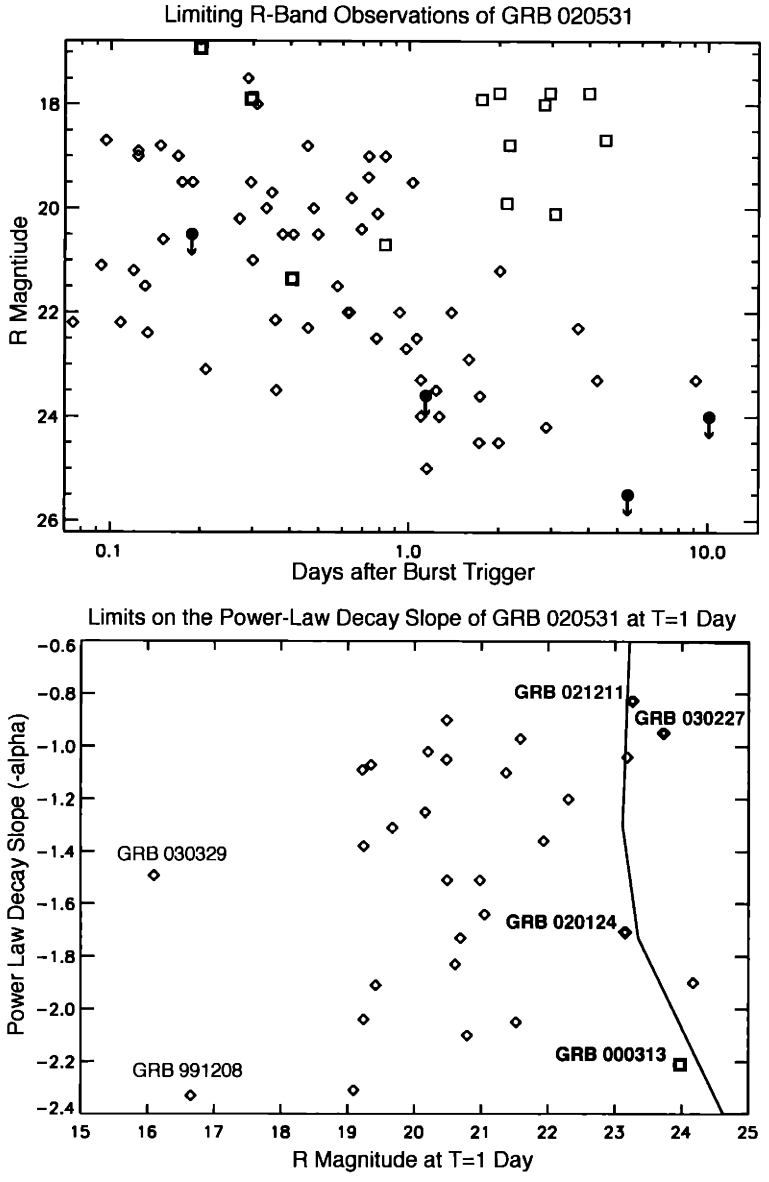

Figure 2-12 *Top panel*: This plot compares the R magnitude upper limits for GRB 020531 (filled circles) from our observations and limiting early observations (Lamb et al., 2002b), to previous R band upper limits for Short GRBs; four IPN Short/Hard GRBs (Hurley et al., 2002a, squares), and the *BATSE* Short GRB 000313 (Castro-Tirado et al., 2002a, bold squares). Also plotted are the most limiting measurements for each observed, but undetected, Long GRB since 2000 (diamonds, data from the GCN). *Bottom panel*: The shaded area describes the region of undetectable afterglows as limited by our observations of this burst and earlier limits from the GCN (Lamb et al., 2002b; Li et al., 2002) compared to measured Long GRB afterglows (Figure 2-2), and the decay limit (Castro-Tirado et al., 2002a) for the optical flash coincident with the Short GRB 000313.

or optical, therefore it is unlikely that any of these objects are associated with GRB 020531.

2.4.6 Conclusions for GRB 020531

No conclusive evidence has been found which points to an afterglow associated with GRB 020531. Sources which were followed up in detail were either inconclusive, or definitely not associated with the GRB. In particular, none of the fading *CXO* sources examined in the optical were determined to be transient. Comparing early optical upper limits reported to the GCN (Lamb et al., 2002b) for GRB 020531 and our deeper, later observations to Long/Soft GRB afterglow searches also in the GCN, we can constrain the afterglow of this burst as deeply as almost all other "Optically Dark" Long GRBs reported (see Section 2.2.3), and deeper at late time than any other Short GRB (Figure 2-12, top). If the afterglow of GRB 020531 is assumed to follow the same general power-law decay as that observed for afterglows of Long GRBs, ie. $F = F_0 t^{-\alpha}$, then the allowed lightcurves can be constrained to the region shown in Figure 2-12, bottom. Specifically, our observations have constrained the afterglow of this short burst to fainter than $R \sim 23$ at one day for $0.8 < \alpha < 1.8$, the range in which most early decay slopes for Long GRBs are measured, and the earlier observations by Lamb et al. (2002b) and Li et al. (2002) constrain the afterglow to much fainter limits for $\alpha > 1.8$.

2.5 The Optically Dark GRB 030115

HETE (Section 1.3) detected GRB 030115 (=H2533) (Kawai et al., 2003b) on January 15, 2003, at 03:22:34 UT. A refined ground analysis of the WXM position was reported to the GCN at 04:33:07 UT, and a 2′ error radius SXC position was reported at 04:46:34 UT, only 1.4 hours after the burst. Followup optical observations were begun early, with observations as deep as the DSS beginning between 1-2 hours after the burst, (Atteia et al., 2003c; Castro-Tirado et al., 2003b; Masetti et al., 2003a), but no conclusive evidence for a fading counterpart was found. Infrared (IR) observations were begun at ∼5 hours after the burst by Levan et al. (2003) and a fading IR source was reported to the GCN about 15 hours after the burst.

We made IR observations of this source at the Magellan Observatory (Section 1.4.1) with Classic Cam on January 23, 2003, but we were not able to fully analyze the data because of difficulties with the astrometry of the images. The release of archived (Section 1.4.3) *HST* NICMOS and ACS (Section 1.4.2) observations of GRB 030115, taken as part of the Cycle 11 *HST* observing program #9405, allowed for more accurate astrometric calibration of our images. Our analysis of the Classic Cam images and the public *HST* data is presented below.

2.5.1 Infrared Data and Analysis

The USNO catalog star ∼14" to the West of the GRB was used to align the telescope with the field. At the time of our observations, however, it was discovered that there were engineering issues with the telescope and the camera rotation angle could not be determined. With only one bright star in the field of view, it was impossible to determine the orientation of the field. Stacking of the 45 good images from the data set revealed three other weak sources in the field, but the 2MASS images of the field did not even resolve our guide star. A finder chart available from Levan et al. (2003), and did show faint sources around the guide star, but it was possible that one of the faint sources in our images was the GRB afterglow, confusing the matter.

The release of three *HST* NICMOS *F*160*W* filtered images from February 10, 2003, covering the field of GRB 030115 gave a much better opportunity to orient our images, as the *HST* images were much deeper and so clearly resolved many faint sources around the guide star. We stacked the three images in IRAF with *imcombine* discarding the maximum pixel at each position to remove cosmic rays. We found that the Classic Cam image was in fact rotated by 180 degrees from the rotation recorded in the header. A comparison between the stacked NICMOS image and our Classic Cam image (Figure 2-13) shows the corrected orientation. Unfortunately, the GRB was below the sensitivity limit for our observations. The limiting magnitude was Ks=22 for the 45 x 60 second stacked Classic Cam image. We used the IRAF *apphot* package to measure a magnitude of 24.8 for the host galaxy in the *F*160*W* filter (∼*H* band) in the NICMOS image. This magnitude was calibrated using the zero point photometry keywords in the *HST* header files of the images.

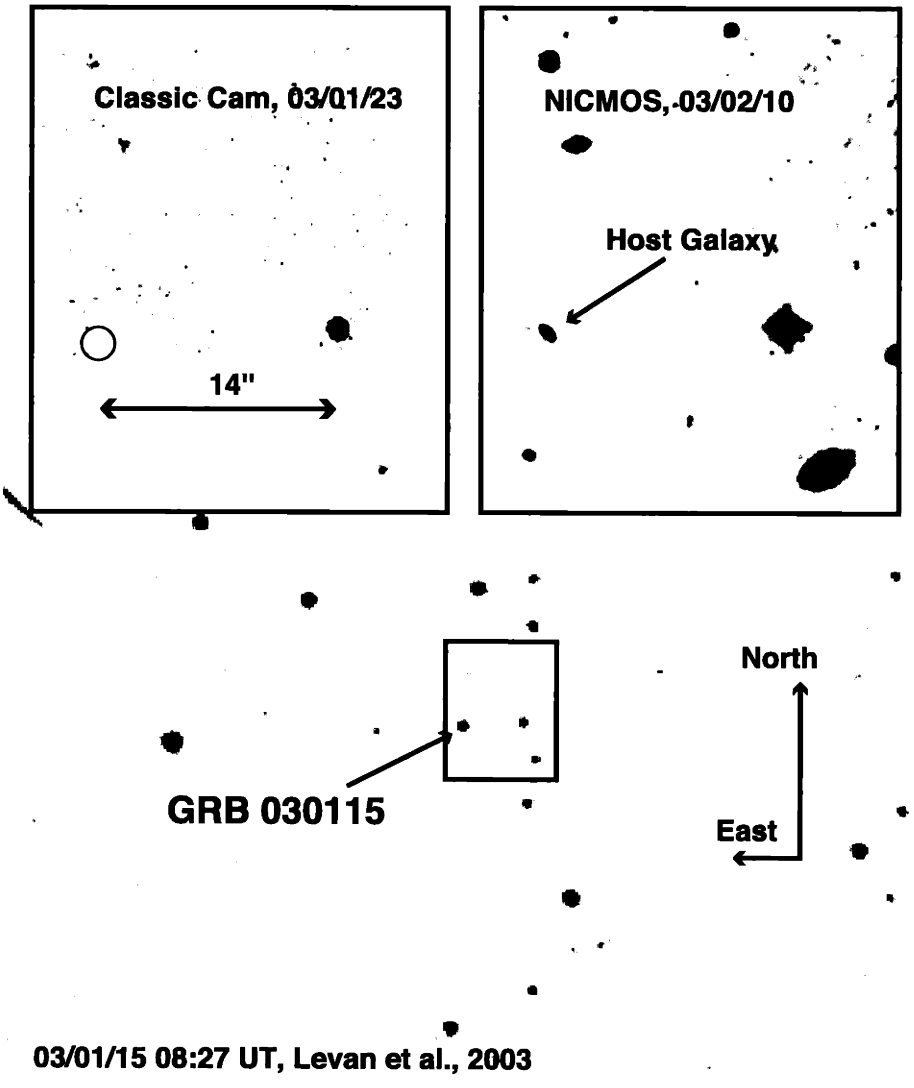

Figure 2-13 A comparison of the ClassiCAM stacked image (left) and the *HST* NICMOS stacked image (right), to the deepest finder chart available; the afterglow discovery image posted by Levan et al. (2003).

Figure 2-14 A two color image made from the *HST* ACS $F606$ and $F814$ images with cosmetic cosmic ray cleaning performed. The galaxy is blue and irregular, with a small companion to the North East. The bright star is the guide star used in our Classic Cam observations (Figure 2-13). The large image is about 30″ wide, with North up and East to the left.

2.5.2 Optical Data and Analysis

The IR transient was reported to the GCN ~16 hours after the burst (Levan et al., 2003). At that time earlier observers were able to re-examine their images, and the transient was found in the optical at R ~21.5 on January 15, 2003, at 05:25 UT (Masetti et al., 2003b) with respect to the nearby USNO-A2 catalog star at R=18.8. Late time optical observations were made by Garnavich (2003) on Jan. 29.4 UT, 2003, and they measured the magnitude of the GRB and host at $R = 24.5$, also using the same USNO-A2 star. Our observations are calibrated against the USNO-B1 catalog, in which this star is reported to have a magnitude of R=19.450, so we have adjusted for this in our comparisons.

The public archived ACS images we obtained were also taken on February 10, 2003. There were OTFR (Section 1.4.3) images available in two filters, $F606W$, the wide band VR filter, and $F814W$, equivalent to the Johnson-Cousins I filter. Only one image was available in each filter, so we could not perform cosmic ray rejection by summing images. We performed aperture photometry in IRAF on the GRB host galaxy in each of the two ACS images. A 5 pixel (0.25") radius aperture, smaller than the galaxy, was used to avoid contamination by cosmic rays. Using the flux calibration keys in the headers of the images, we find a magnitude of ~26 for the central region of the host galaxy in both filters, $F606W$ and $F814W$. Using this photometry, we calculated the surface brightness of the galaxy in both bands as ~24 magnitudes per square arcsecond. The galaxy is small, blue and irregular compared to the other galaxies in the field (Figure 2-14. The small companion to the host galaxy at 1.3" to the Northeast, reported by Garnavich (2003), is also resolved in

these images. Using the same 5 pixel radius aperture, we measure its magnitude at ~26.3 in $F606W$ and ~27 in $F814W$.

2.5.3 Conclusions for GRB 030115

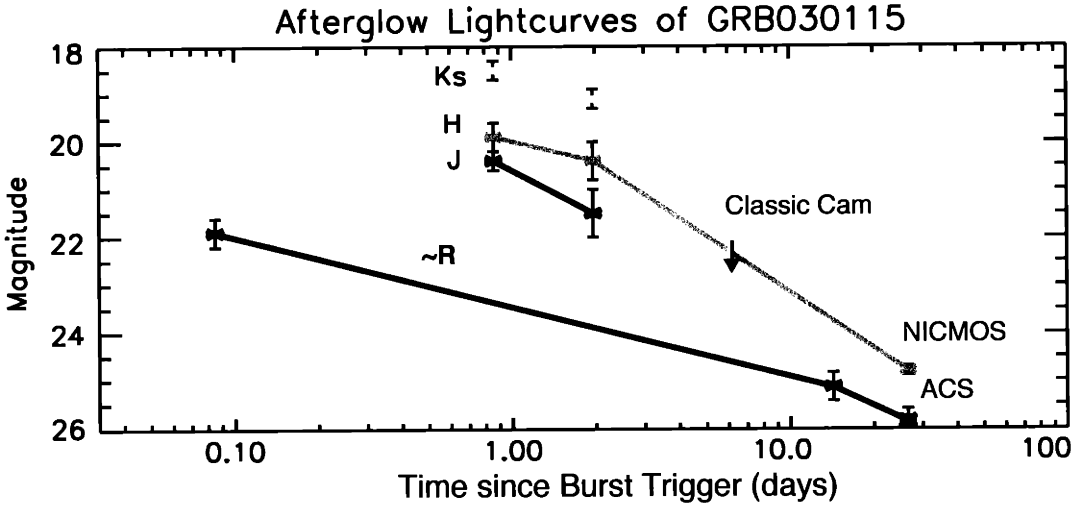

Figure 2-15 An updated lightcurve for GRB 030115, plotted using data from GCN (Kato et al., 2003b; Masetti et al., 2003b; Garnavich, 2003) and including the new points from Classic Cam and *HST* .

We can place a new upper limit in the afterglow of GRB 030115 of Ks > 22 on January 23, 2003. This upper limit is too faint to be consistent with the afterglow decay of α ~0.7 between the two earlier Ks measurements reported by Kato et al. (2003b), which implies a steepening of the light curve at some time between ~2 and 6 days after the burst. We also measured the magnitude of the host galaxy in $F160W$ (~H band) to be 24.8 magnitudes, 25 days after the burst. Optically, the host galaxy of GRB 030115 is seen to be a small, irregular galaxy, perhaps interacting with the small galaxy to the Northeast. A slight count excess at the position of the GRB in the Digital Sky Survey (DSS) image of the region was reported by Masetti et al. (2003b), but this is most likely noise, given the faintness of the host galaxy in the ACS images. A photometric redshift of z~2.2 for the host galaxy was reported by A. Fruchter during the 2003 Gamma Ray Burst Symposium in Santa Fe, NM, using the ACS *HST* images. Therefore, optical afterglow of GRB 030115 was most likely faint due to extinction in its own host galaxy, and not due to high redshift Lyman α absorption.

2.6 GRB 030418

GRB 030418 (=H2686) (Shirasaki et al., 2003a) was observed on 09:59:18.85 UT, April 18, 2003, by HETE FREGATE and WXM. GRB 030418 had a T_{90} of ~135 seconds, and showed two distinct periods of emission (Figure 2-17). It clearly shows the classic GRB prompt evolution of hard to soft between the two peaks, with the first peak brighter than the second in the FREGATE C Band (30-400 keV) and the second peak brighter in the WXM (2-25 keV). The burst was X-ray rich, with a flux ratio, $S_x/S_\gamma = 0.5$, and the strong signal in the WXM gave a good flight location, which was sent out over the GCN only 215 seconds after the trigger time. This burst occurred during the full moon, and so the SXC was off due to optical light contamination (see Section 1.3.1 for an explanation of the SXC). The WXM ground location was reported at 104 minutes after the burst and had an error radius of 9′.

Early follow up observations were begun automatically with robotic telescopes after the first GCN notice, but not examined until later (see Conclusions for GRB 030418). An afterglow candidate was found a few hours after the burst, at R=18.8, by Price et al. (2003a), and confirmed an hour later to be fading (Price et al., 2003b). We initiated an internal ToO for the upcoming MIT time Magellan, which was to begin 2 days later.

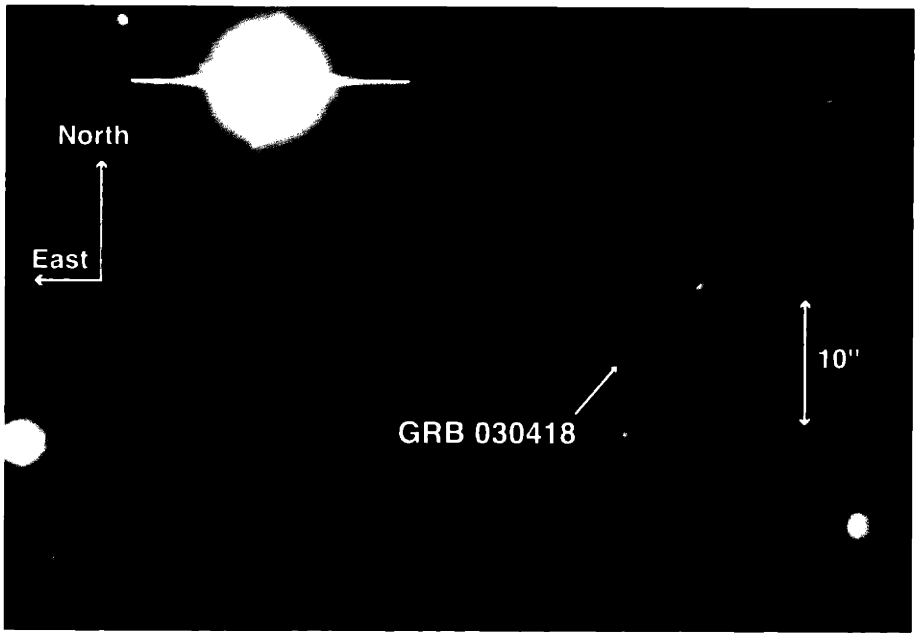

Figure 2-16 This RGB image was made with the I and stacked R band images from 2.6 days after the burst as red and green, respectively. The V band image from 6.6 days after the burst was used as the blue for the background sources, but with an estimated magnitude of V=23.5 for the afterglow to give a realistic color for 2.6 days after the burst. We assumed that the V band afterglow followed the decay curve measured in R, and used the magnitudes measured at 6.6 days to get $V - R$.

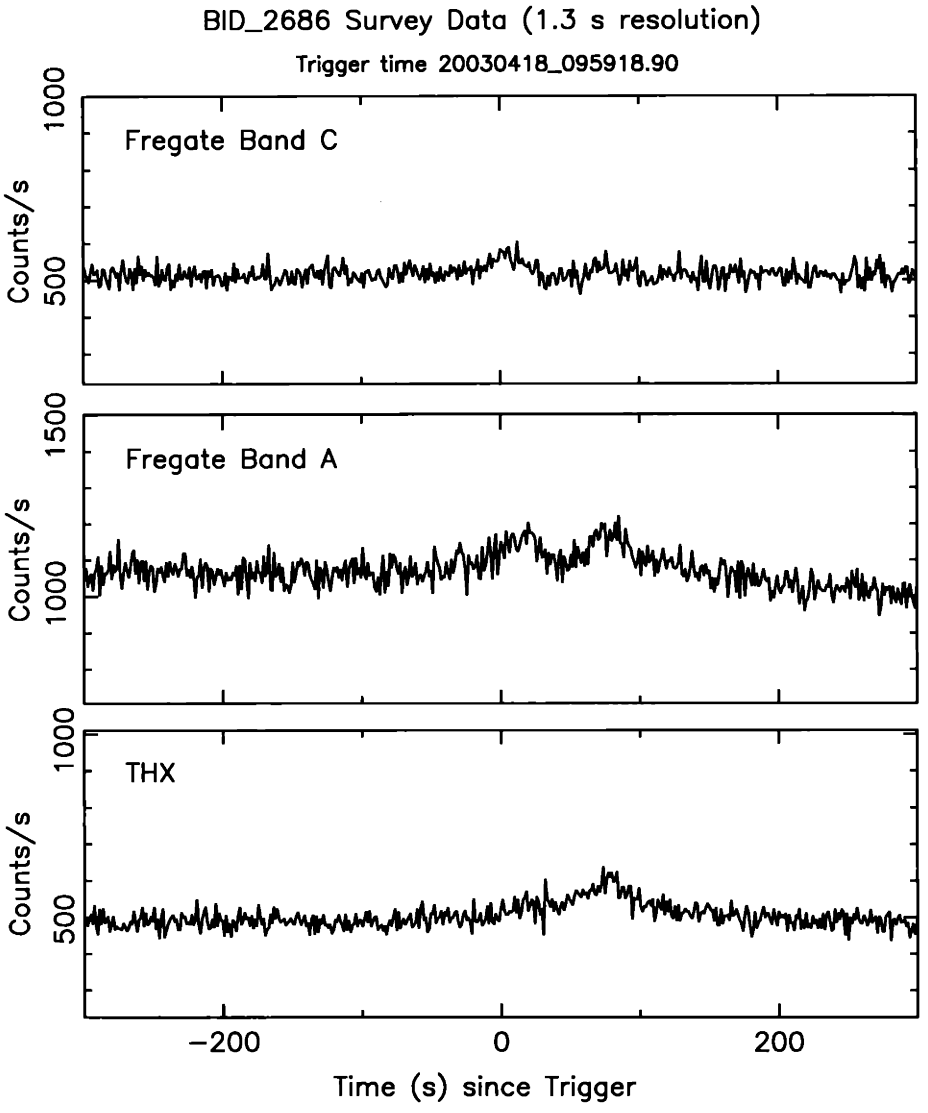

Figure 2-17 The light curve of GRB 030418 (=H2686) in FREGATE bands A (8-40 keV) and C (30-400 keV), and the WXM (2-25 keV) shows spectral evolution from hard to soft between the two peaks.

2.6.1 Optical Observations with Magellan

We used the Clay 6.5 meter telescope at Magellan with the MagIC instrument for these observations. Because the position of the optical counterpart was known, the small FOV and high resolution (see Section 1.4.1) of MagIC were optimal. On the first night of observations, 2.6 days after the burst, we imaged the afterglow in the Harris R three exposures of 300 seconds and in the I for one exposure of 300 seconds. We observed the burst again 4 days later, 6.6 days after the burst, with two 400 second exposures in Harris R, and one each in V and I. The images were bias corrected with frames taken each night. The afterglow had faded by more than 1.5 magnitudes during the 4 days and it was below the limiting magnitude in the I band. Unfortunately our second observations did not have as good seeing as the first, so the limiting magnitude was about half a magnitude higher.

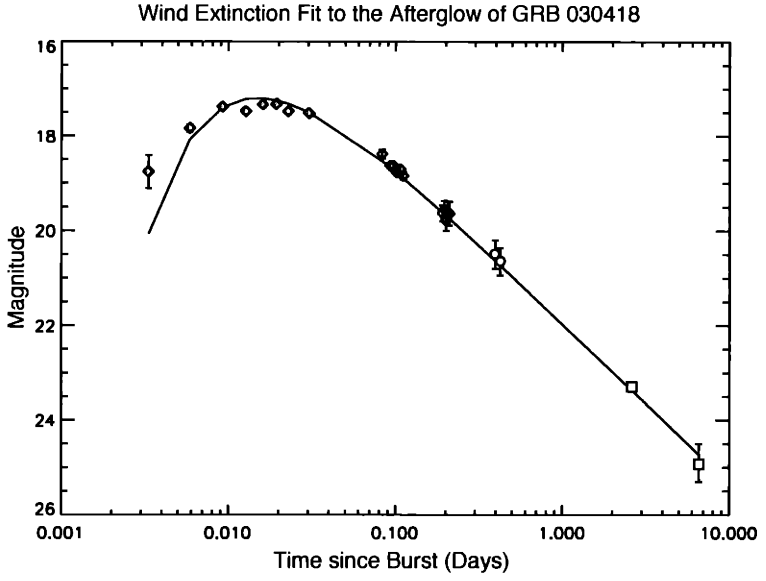

Figure 2-18 The R band lightcurve for the afterglow of GRB 030418 adapted from Rykoff et al. (2003), including their early observations of the burst with ROTSE (filled diamonds) and Sliding Springs (open diamonds), and the later observations reported to the GCN (Ferrero et al., 2003; Dullighan et al., 2003a) (circles, squares). Rykoff et al. (2003) fit the afterglow lightcurve to a stellar wind absorption model where $F = F_0 t^{-\alpha} e^{-\beta_t/t}$.

2.6.2 Conclusions for GRB 030418

The field of GRB 030418 was observed at early times by the ROTSE-III array of small robotic telescopes, which observed the rise of the optical afterglow for this burst with its wide field ($\sim 2°$), unfiltered, 0.45m telescopes and subsequently by the 40in telescope at Sliding Springs Observatory (Rykoff et al., 2003). At late times the burst was also observed at the 152 cm telescope in Loiano (Ferrero et al., 2003) before

our observations at Magellan (Dullighan et al., 2003a) (Figure 2-18). The rise of the lightcurve is fit reasonably well by a power-law decay with extinction at early times by a massive star's stellar wind, as described in (Rykoff et al., 2003). The slope of the power-law decay is constrained by our late time observations and those of Ferrero et al. (2003) to $\alpha = 1.36 \pm 0.01$. The wind-extinction model assumes a pre-burst stellar wind surrounds the collapsing star and is described by a density profile $\rho = \rho_0 r_0^2/r^2$ and optical depth $\tau = \beta_r/r$. As the shock front moves out through the wind with Lorentz factor Γ, the optical depth changes as $\tau = \beta_r/\frac{1}{2}\Gamma^2 ct = \beta_t/t$, and therefore the extinction of the afterglow will go as $e^{-\beta_t/t}$. The mass loss rate indicated by the fit of Rykoff et al. (2003) is typical of a massive star progenitor used in the collapsar models of Woosley (1993) and Zhang, Woosley, & MacFadyen (2003) (Section 1.1.5).

2.7 XRF 030723

XRF 030723 (=H2777) (Prigozhin et al., 2003) was detected at 06:28:17.45 UT on July 23, 2003 by *HETE* . This soft burst had an $E_{peak}$of about 13 keV. The burst was triggered in the 2-25 keV band by the WXM instrument, but the burst was seen in all three instruments, Fregate, WXM, and the SXC. A flight WXM localization was sent out at 42 seconds after the trigger with a 30 arcminute radius, and a preliminary ground SXC location was distributed ~7 hours later. The final SXC error circle was distributed in a GCN Circular (Prigozhin et al., 2003) and had a 2′ radius. As XRFs (Section 1.1.4) are still not well understood, the HETE Science team at MIT immediately initiated ToO observations of the SXC error circle in the optical at the Magellan Observatory in Chile, and in the X-ray with *CXO* (Butler et al., 2004).

2.7.1 Optical Observations with Magellan

Our observations of XRF 030723 were made as an exchange with observers from Harvard University who were then using the Magellan Clay telescope. They agreed to image the field of the burst for our use, in return for make-up observations during the subsequent MIT time. The imaging took place on July 24.31 UT, 1.04 days after the burst and at that time the afterglow of XRF 030723 had not yet been discovered. The field of the SXC error circle was imaged with the LDSS2 instrument in the Harris R band for four exposures of 360 seconds each (Table 2.1) and stacked to clean cosmic rays and improve sensitivity. We compared our observations to the DSS (Section 1.4.3) to search for new sources, but none were new sources were found, down to the limiting magnitude ($R \sim 20.5$) of the DSS.

The first *CXO* observations took place two days after the burst (Butler et al., 2004) and the positions of the bright sources was compared to our optical observations. The brightest source in the *CXO* observations had a counterpart in our images at $R = 21.13 \pm 0.05$. A report was made to the GCN three days after the burst by Fox et al. (2003b) of a fading source inside the SXC error circle. This counterpart matched the bright *CXO* source to within 0.7″ (Butler et al., 2004) and we reported our optical magnitude for the counterpart to the GCN (Dullighan et al., 2003b). A second epoch of optical imaging was made on July 28.39 UT, 5.13 days after the burst, with the MagIC instrument. Three 200 second images were taken, and summed to clean cosmic rays. The OT was detected at 24.2 magnitudes (Dullighan et al., 2003c), very close to the limiting magnitude of the observations.

2.7.2 Conclusions for XRF 030723

To date, few of the detected afterglows of XRFs have lightcurves more detailed than two points confirming a fade. XRF 030723 is one of these few, and details of its lightcurve have been fit to a two component jet model by Huang et al. (2003). This model attributes the specific variations seen in the lightcurve to the observer's view of the burst's jet configuration. The two component model proposes a narrow jet of $\theta \sim 0.1$ width, at a highly relativistic speed ($100 < \Gamma < 1000$), carrying the majority

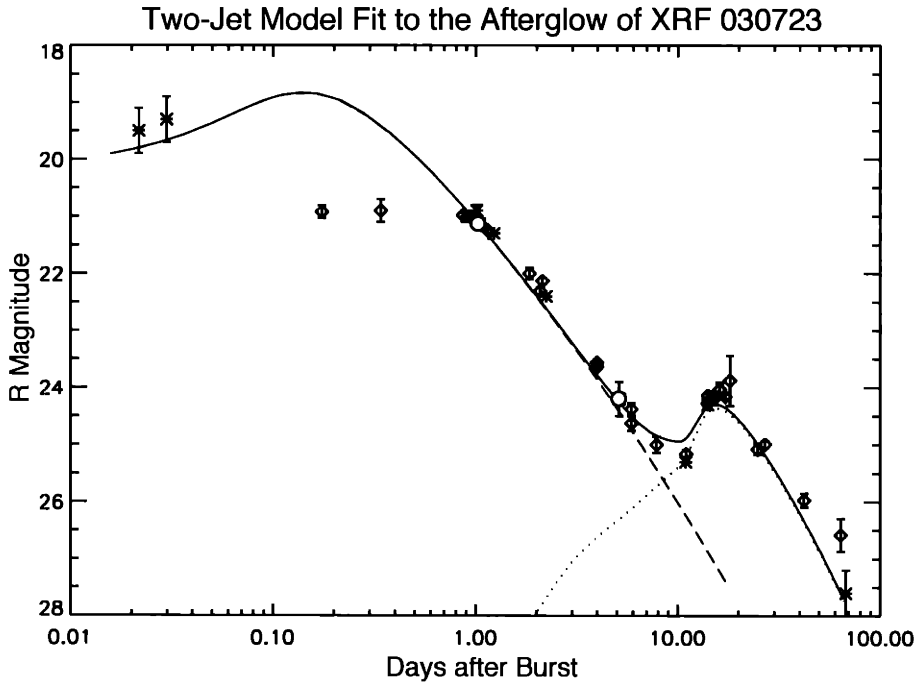

Figure 2-19 The two-jet model lightcurves for XRF 030723 are taken from Huang et al. (2003), with the observations from the GCN (Smith et al., 2003; Bond, 2003; Fox et al., 2003b; Fynbo et al., 2003b; Kawai et al., 2003c, stars), our data (Dullighan et al., 2003b,c, circles), and the new points from (Fynbo et al., 2004, diamonds) overplotted. The dashed line is the emission from the wide angle jet (θ=0.3, Γ=30) and dotted line is for the narrow angle jet (θ=0.09, Γ=300). The viewing angle of the observer for this fit is θ=0.37 (Huang et al., 2003).

of the energy, and a wider jet of $\theta \sim 0.3$ with a slower speed ($10<\Gamma<100$) Huang et al. (2003). This setup can explain the range of E_{peak} seen for GRBs by moving the viewing angle of the observer. The farther one looks off axis, the less energetic the initial outburst will seem. For the duration of the prompt emission, the observer's view is restricted to a narrow region, due to relativistic beaming. During the afterglow phase, this region is expanding, and if the observer's view was original only of one jet, eventually the other jet will come into view. For an XRF, we begin the observations at a high viewing angle with only the wider, less energetic jet visible. Initially, the afterglow rises as the relativistic beaming decreases and more of the wide jet comes into view, and then starts to fade as the jet decelerates and loses energy. Finally the more energetic, narrow jet becomes visible and causes a rebrightening of the afterglow. This model is a good fit to the original data available from the GCN for XRF 030723, but new data published recently by Fynbo et al. (2004) do not fit this model between 0.1 and 0.5 days (Figure 2-19).

Recently, a preprint by Fynbo et al. (2004) was published using extensive observations not reported to the GCN. They also measure a late time rise in the lightcurve

of XRF 030723, but fit it to a SN lightcurve (Figure 2-20). The SN used is not as highly energetic as that used for most GRB, SN bumps, but a more typical Type Ic SN 1994I. If the association is correct, it suggests that XRFs may occur in the collapse of slightly less massive stars. An intrinsic spread in progenitor mass may account for the spread in energy between Long GRBs and XRFs. They do not fit the very early rising data from Smith et al. (2003), however. Fynbo et al. (2004) found the best fit to the powerlaw subtracted bump using the lightcurve of SN 1994I scaled to z=0.6. Interestingly, this redshift almost exactly equal to that estimated (z=0.59) by Atteia et al. (2003b) when fitting the for the redshift of the burst using the Amati relation (Amati et al., 2002, Figure 1-4).

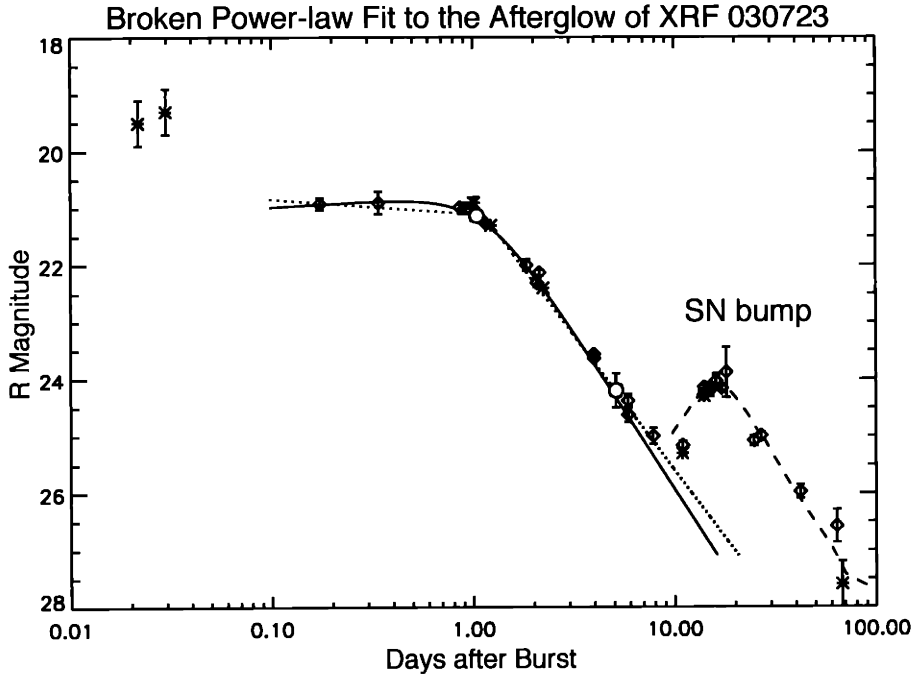

Figure 2-20 This model lightcurve of XRF 030723 is taken from Fynbo et al. (2004), and shows a fit of their data to two variations on a broken power-law fit, followed by a scaled SN lightcurve peaking about 20 days after the burst. The same data points used in Figure 2-19 are overplotted.

2.8 GRB 030725

Close on the heels of XRF 030723, GRB 030725 (=H2779) (Shirasaki et al., 2003b) was detected by *HETE* at 11:46:24 UT on 25 July 2003. This burst was quite bright, but too near the edge of both the WXM and SXC Y-cameras for flight localization. Ground analysis was necessary before the elongated $10 \times 30'$ WXM location was distributed at 13:19:34 UT. Fortunately, the burst was bright enough to be detected by the SXC X-Camera, and so a smaller SXC 1-D error region with a $3'$ width, but the same length, was also derived and distributed in the GCN notice at 16:07:46 UT. Many of the professional telescopes around the globe were still tied up observing XRF 030723, and so the early afterglow search for this burst was mainly among the American Association of Variable Star Observers (AAVSO) International GRB Network. A fading optical counterpart for this GRB was reported to the GCN at 02:27:14 UT, July 26 (Monard, 2003a). This was the first discovery of a GRB afterglow by an amateur astronomer. The OT was slightly outside the SXC 90% error region reported to the GCN, but within the 99% error region.

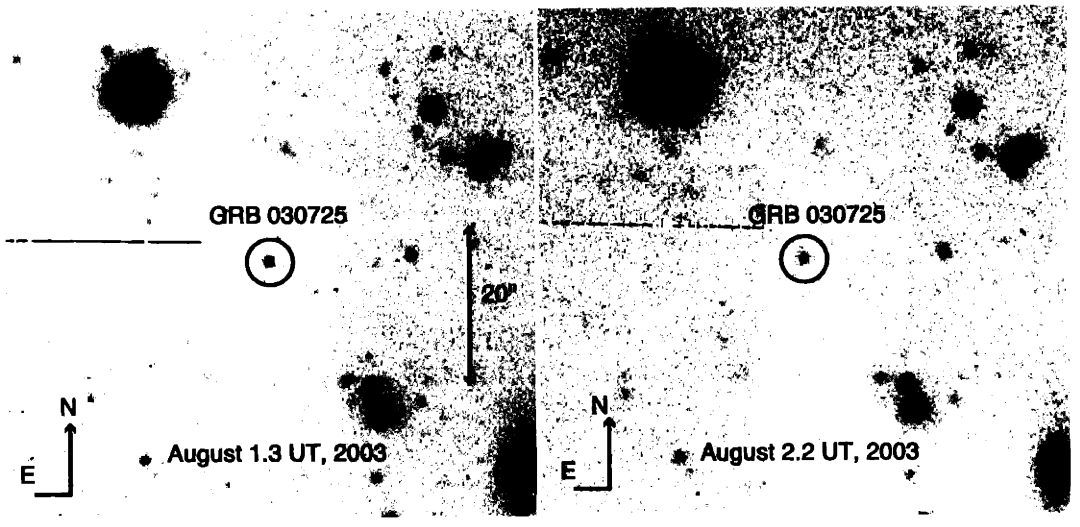

Figure 2-21 The two r' band observations of GRB 030725 with MagIC on the Magellan Clay 6.5m telescope. The images have been binned to a quarter of the original pixel size for clarity. The afterglow of GRB 030725 is in the center of both images.

2.8.1 Optical Observations with Magellan

Observations were made with the MagIC instrument on the Clay 6.5 meter telescope on two nights, August 1.305, and 2.166 UT, 2003 (Table 2.1). The observations were made as Target of Opportunity interventions and so were taken in the Sloan r' filter as the Sloan filter set was in use at the time. Each observation consisted of two exposures that were later stacked to increase sensitivity. The first night, two 300 second exposures were taken and on the second night the exposure time was increased

to 360 seconds. Bias images for MagIC and flat-field images in the r'-Band were taken as part of the general observing routine and were used to reduce the four images after they had been retrieved to MIT, at the end of the observing run. The afterglow of GRB 030725 was observed to fade by about 0.3 magnitudes in r' between the two observations, starting at $r' = 22.25 \pm 0.05$ on the first night and fading to 22.55 ± 0.05 on the second.

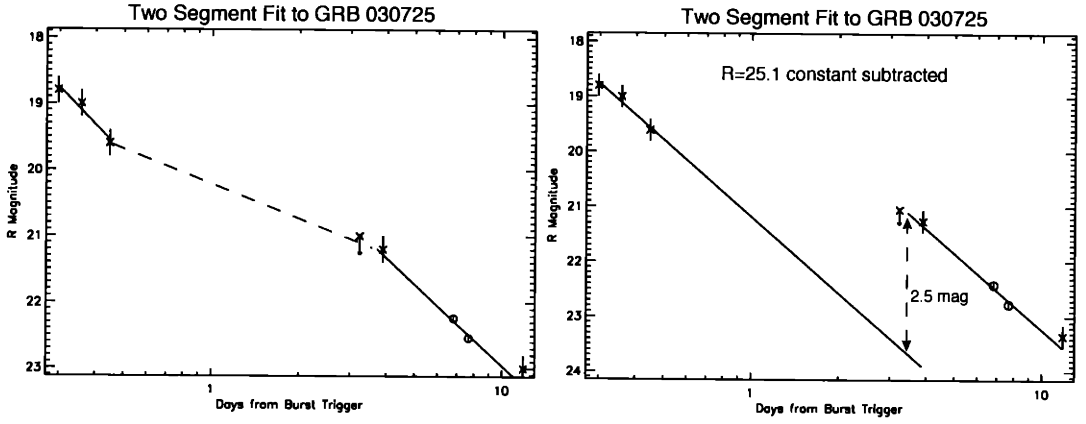

Figure 2-22 *Left panel*: The optical afterglow lightcurve of GRB 030725. Our observations (Dullighan et al., 2003d) are marked with circles, and the rest are from the GCN (Monard, 2003a,b; Vinter et al., 2003; Jorgensen et al., 2003). We added 0.2 magnitude errors to the observations with no errors reported. We fit the two segments of the lightcurve separately, and find that the later segment is slightly shallower than the first. *Right panel*: The same fit to the afterglow observations, but with a 25.1 magnitude source subtracted from all the data. Now both segments follow the same decay rate, $\alpha = 1.85 \pm 0.15$, with an offset of 2.5 magnitudes between them, giving a χ^2 of ~ 4.5.

2.8.2 Conclusions for GRB 030725

We fit the lightcurve of GRB 030723, using our data in conjunction with that available from the GCN (Monard, 2003a,b; Vinter et al., 2003; Jorgensen et al., 2003). The GRB afterglow was not observed between 0.5 and 2 days after the burst (Figure 2-22). During that time, a flattening, or re-brightening of the optical afterglow likely occurred, as the data are best fit by two slopes, $\alpha = 1.8 \pm 0.5$ for the first, and $\alpha = 1.6 \pm 0.2$, with a total χ^2 of ~ 4. If a constant source of 25.1 magnitudes is subtracted from the observations, then all the data is fit by a decay of $\alpha = 1.85 \pm 0.15$ ($\chi^2 \sim 4.5$), with an offset of 2.5 magnitudes, or a flux increase of ~ 10, between the two segments. This is similar to the period of refreshed shocks in GRB 030329 (Section 1.2.3), modeled by Granot, Nakar, & Piran (2003), which also brightened the afterglow flux by a factor ~ 10 over the first few days, with the decay returning to the original slope after each rise. Without afterglow measurements during the

presumed rising phase, between $\sim$ 1 and $\sim$ 3 days, it is difficult to confirm this finding. The data also can be fit reasonably well to a single power law with a decay slope $\alpha = 1.03 \pm 0.04$ (Figure 2-23). A 0.5 magnitude rise and then a return to the original fade, due to a smaller over-density in the jet or surrounding medium, could explain the data variation around 3 days. Without a more detailed lightcurve, however, it is difficult to draw any specific conclusions.

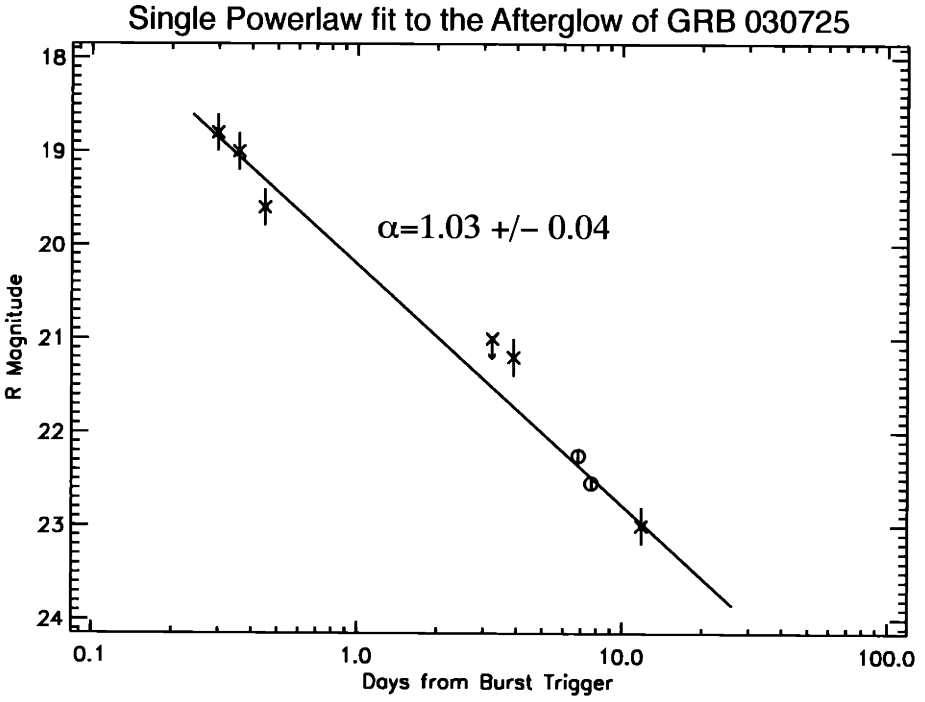

Figure 2-23 The lightcurve of GRB 030725 can be fit to a single powerlaw of $\alpha = 1.03 \pm 0.04$, and a χ^2 of $\sim$ 8, if the measurement at 3 days (Vinter et al., 2003) is excluded. A 0.5 magnitude excess is seen at 3 days, but could be due to a smaller fluctuation in the lightcurve than that assumed in Figure 2-22.

Chapter 3

Thesis Summary

In the past seven years, afterglows have grown from a prediction of the current model, to the focus of the GRB field. Except for the break energy, prompt GRB spectra lack features and, beyond the Long/Short split, the lightcurves of GRBs have proved difficult to classify. The future of GRB science will likely continue to stem from detailed studies of afterglows. *HETE* was designed with the idea of facilitating rapid followups at longer wavelengths, with most of its collecting area involved in X-ray localization, and with automatic reduction and dissemination of localizations through the burst alert stations and GCN. *HETE* also points in the anti-solar direction, so as to maximize the dark time for optical observations. The observing community has made good use of *HETE* 's speed to catch GRB afterglows early and often. All but one of the 15 GRBs with small SXC 2′ error circles have had an optical counterpart found. Robotic observations have shown that early rises and decays of afterglows do not follow a single model. Detailed late time observations have marked jet breaks, refreshed shocks, and SN rises. The *HETE* detection of GRB 030329 has confirmed the link between GRBs and SN, with the spectrum of SN 2003dh emerging from the afterglow after 10 days, and dominating the lightcurve at late times (Section 1.2.4). Also, afterglow observations of *HETE* XRFs, which were only recently discovered, are confirming the link between these events and Long GRBs(Section 1.1.4).

This thesis covers a wide range of afterglow phenomenon, and a single conclusion is difficult to draw, therefore the results and conclusions for each afterglow studied have been summarized below. Each observation is a sample drawn from a population we are only beginning to understand and is part of the collective effort to narrow this gap. Lightcurve modeling of the afterglows we observed has drawn connections between massive stars and GRBs on multiple fronts, evidencing stellar wind extinction in GRB 030418, a SN rise in XRF 030723, and possible shocks in GRB 030725. Models are also beginning to form through cross referencing of prompt and afterglow classification. Jet breaks modeling suggests a standard energy for prompt events (Section 1.1.3), and the same authors (Bloom, Frail, & Kulkarni, 2003) have also suggested a link between low energy prompt events and fast fading afterglows. Measuring the redshifts of more events is critical to these studies, so as to flesh out the populations.

We imaged GRB 020331 (Section 2.3) on three occasions with Magellan, twice with LDSS2 at 0.53 and 8.3 days after the burst, and MagIC at 12.5 days (Table 2.1).

The Optical Transient (OT) associated with GRB 020331 is measured at all three epochs. Combined with photometry published in the GCN we measure a smoothly decaying lightcurve after removal of contaminating sources, with $\alpha = 0.97 \pm 0.02$ and no break detected between 0.53 and 43 days after the burst. To fit this decay we subtracted a presumed underlying host galaxy of $R = 26.0 \pm 0.1$ beneath the OT. A late time rise in the lightcurve between 43 and 50 days after the burst was detected by Soderberg et al. (2002a) in *HST* STIS Clear images. We confirmed this flux excess in the next *HST* exposure taken 139.6 days after the burst, measuring the magnitude of OT+host to be 25.2 ± 0.1 in the STIS Clear Filter, which gives a shallow fade of only $\alpha \sim 0.65$ between the last two points.

We imaged the NIR source associated with GRB 030115 (Section 2.5) with the IR imager ClassicCam in the K-short band at Magellan, 6.0 days after the burst. The afterglow position was known to arcsecond accuracy at that time, but the orientation of the camera was not known. We could not clearly match the single bright source and three very faint sources in our $29'' \times 29''$ images to any available finder charts until *HST* NICMOS images covering the same field were released a few months later. The images were aligned, but the NIR afterglow was below the limiting magnitude of our images. A break in the lightcurve must have occurred between 2 and 6 days, for the limit of Ks$<$ 22 we measure at 6 days is 2 magnitudes below that projected by the fade of $\alpha \sim 0.7$ measured earlier Kato et al. (2003b). We also measured the magnitude of the host galaxy of GRB 030115 in the late time *HST* NICMOS and ACS images, finding $H \sim 24.8$ and $R \sim 26$.

The OT of GRB 030418 (Section 2.6) was found a few hours after the burst and confirmed to be fading. We imaged the OT at Magellan with MagIC on two nights, 2.6 and 6.6 days after the burst, in I and R on the first and I, R, and V on the second night (Table 2.1). The afterglow is seen to fade smoothly as a power law, with a slope of $\alpha = 1.36 \pm 0.01$, in all the observations after ~ 0.1 days. No observations after our second epoch at 6.6 days have been reported, so the late time decay of this burst is not known. Early observations with ROTSE-III observed the rise and wide peak of the optical emission before 0.1 days. Their model of stellar wind optical extinction (Rykoff et al., 2003) fits the shape of the early light curve better than a pure, synchrotron model lightcurve (Sari, Piran & Narayan, 1998), implying that the progenitor of the burst was a massive star undergoing mass loss through its stellar wind.

XRF 030723 (Section 2.7) was the first XRF to have its optical counterpart discovered within a few days after the burst. We were able to confirm the candidate OT of Fox et al. (2003b) in our observations with *CXO* and measured its magnitude in the optical at 1 day and 5 days after the burst (Table 2.1). The burst lightcurve rises sharply after 10 days, and then fades again. Two models have been proposed to fit this late time bump. The first is an off-axis, structured jet model with a soft spectrum, wide, outer jet and narrow, energetic, inner jet. An XRF prompt event is created by having the observer inside the angle of the wide jet, but outside the narrow jet. The early afterglow then follows the decay of the soft wide jet until the relativistic opening angle of the bright inner jet reaches the viewing angle of the observer, and a re-brightening is observed. The second model follows the standard "uniform" jet

(Section 1.1.3), for the afterglow before ten days, and then models the late time rise as a SN lightcurve. If the second model is confirmed, this would be the first SN seen from an XRF. Either model still ties XRFs closer to GRBs, each being a variant on an accepted GRB afterglow model.

GRB 030725 (Section 2.8) was observed by only a few groups, being overshadowed by XRF 030723. We imaged the afterglow with MagIC at 6.8 and 7.7 days after the burst. Combining our results with the other six data points available from the literature, we find that the decay is not particularly well fit by a smooth power law, even though the lightcurve is sparse. The assumption of a rise in the lightcurve of $\sim$2.5 magnitudes between 1 and 3 days gives a much better fit. This could be due to a period of refreshed shocks in the jet, such as that seen for GRB 030329. Data between 1 and 3 days for the afterglow of GRB 030725 would help to clarify this. Late time observations yielding a host galaxy magnitude could also help to clarify which variations in this lightcurve are intrinstic, as the last point in the lightcurve seems to imply a flattening of the decay.

Two of the *HETE* GRBs we followed up do not have any clear long wavelength counterpart, to date. The first of these was XRF 011212, found early in *HETE* 's mission and before XRFs were well understood in terms of satellite detection or general population. The second was a Short GRB (Section 1.1.6), and to date, no Short GRB has had a confirmed long wavelength counterpart. They are one of the biggest mysteries remaining in the field.

XRF 011212 was detected in WXM survey data on the ground as, at that time, *HETE* was not triggering on XRFs in flight. Follow up observations did not begin until after the location was sent out, about half a day after the burst. This was not fast enough to catch a faint or fast fading afterglow, and our observations rule out any fading source brighter than $R \sim 24$ at 2 days. Faint afterglows could be caused by any number of factors. Extinction of the optical light could occur in either the circumburst medium, which may include thick shells expelled by a massive star progenitor, or thick star forming clouds which may still surround a young massive stellar progenitor, or extinction by chance aligned dust clouds further away in the host galaxy. The external shocks causing an afterglow could also be intrinsically faint, for example if the burst environment happened to be relatively clean, and minimal shocks formed, the afterglow would not be strong.

The Short GRB 020531, was a bright, short ($\sim$ 1 second) burst seen in both FREGATE and WXM on board *HETE* . Short bursts have hard spectra, and ground analysis of the WXM data was needed for a location. The *HETE* team observed this burst both in the optical and with *CXO* , but no conclusive afterglow was seen in either of these regimes. Both observations limit the afterglow of this burst to "faint" by the standards of Long GRB afterglows, but this is consistent with the current theory for their origin. Short GRBs (Section 1.1.6) are thought to occur when two compact objects coalesce, usually either a NS-NS binary or a NS and a BH. These events would occur far from the dense star formation regions where Long GRB progenitors are found, out away from the planes of their galaxies. If the surrounding medium is very sparse, then external shocks will not form, and no post burst emission would be expected at any wavelength.

Future work on any of these bursts would involve late time host galaxy detection or photometric redshift determination, if not already performed. Host galaxy measurements are all that can be done once the afterglow has faded away, but can help to place previous measurements within a significant context. Fitting the current lightcurves to more detailed physical models, in combination with other bursts, will also continue. We are always ready to move for the next 'big' burst, of course, but it is essential to explore each of these burst in as much detail as possible, until eventually a unified picture for the diverse GRB phenomena becomes clear.

Bibliography

Amati, L., et al. 2002, *Astronomy and Astrophysics*, **390**, 8189

Atteia, J-L., et al. 2003, in AIP Conf. Proc. **662**, *Gamma Ray Burst and Afterglow Astronomy 2001*, ed. Ricker, G. & Vanderspek, R. (AIP Press: New York), 17

Atteia, J-L., et al. 2003, to appear in proc., 2003 Gamma Ray Burst Symposium, Santa Fe, NM, (astro-ph/0312371)

Atteia, J-L., et al. 2003, *GRB Circular Network*, 1810

Band, D., et al. 1993, *The Astrophysical Journal*, **413**, 281B

Barraud, C., et al. 2003, *Astronomy and Astrophysics*, **400**, 1021-1030

Berger, E., et al. 2002, *The Astrophysical Journal*, **581**, 981-987

Berger, E., et al. 2003, *Nature*, **426**, 154-157

Bloom, J.S., Kulkarni, S., & Djorgovski, S.G. 2002, *The Astronomical Journal*, **123**, 1111

Bloom, J.S., Frail, D., & Kulkarni, S. 2003, *The Astrophysical Journal*, **594**, 674-683

Boella, G., et al. 1997, *Astronomy and Astrophysics Supplement*, **122**, 299-307

Bond, H.E. 2003, *GRB Circular Network*, 2329

Briggs, M. S., et al. 1996, *The Astrophysical Journal*, **459**, 40+

Brown, T. et al. 2002, in HST STIS Data Handbook, v. 4.0, ed. B. Mobasher, Baltimore, STScI

Butler, N., et al. 2002, *GRB Circular Network*, 1415

Butler, N., et al. 2002, *GRB Circular Network*, 1426

Butler, N., et al. 2003, *The Astrophysical Journal*, **597**, 1010-1016

Butler, N., et al. 2003, Ph.D. Thesis, M.I.T.

Butler, N., et al. 2003, *GRB Circular Network*, 2328

Butler, N., et al. 2003, *GRB Circular Network*, 2347

Butler, N., et al. 2004, to appear in proc., 2003 Gamma Ray Burst Symposium, Santa Fe, NM, (astro-ph/0401020)

Castro-Tirado, A., et al. 2002 *Astronomy and Astrophysics*, **393**, L55-L59

Castro-Tirado, A., et al. 2002, *GRB Circular Network*, 1430

Castro-Tirado, A., et al. 2003, *Astronomy and Astrophysics*, **411**, L315-L319

Castro-Tirado, A., et al. 2003, *GRB Circular Network*, 1826

Costa, E., et al. 1997, *IAU Circular*, 6572.1

Costa, E., et al. 1997, *IAU Circular*, 6576.1

Delle Valle, M., et al. 2003, *IAU Circular*, 8197.2

Dermer, C. D., Chiang, J., & Bottcher, M. 1999,*The Astrophysical Journal*, **513**, 656

Dickinson, M. E. et al. 2002, in HST NICMOS Data Handbook v. 5.0, ed. B. Mobasher, Baltimore, STScI

Djorgovski, S.G., et al. 1997, *GRB Circular Network*, 289

Dullighan, A., et al. 2002, *GRB Circular Network*, 1324

Dullighan, A., et al. 2002, *GRB Circular Network*, 1339

Dullighan, A., et al. 2002, *GRB Circular Network*, 1346

Dullighan, A., et al. 2002, *GRB Circular Network*, 1382

Dullighan, A., et al. 2002, *GRB Circular Network*, 1434

Dullighan, A., et al. 2003, *GRB Circular Network*, 2236

Dullighan, A., et al. 2003, *GRB Circular Network*, 2326

Dullighan, A., et al. 2003, *GRB Circular Network*, 2336

Dullighan, A., et al. 2003, *GRB Circular Network*, 2384

Dullighan, A., et al. 2004, to appear in proc., 2003 Gamma Ray Burst Symposium, Santa Fe, NM, (astro-ph/0401062)

Ferrero, P., et al. 2003, *GRB Circular Network*, 2284

Fishman, G.J. & Meegan, C.A. 1995, *Annual Reviews of Astronomy and Astrophysics*, **33**, 415458

Fox, D., et al. 2001, *GRB Circular Network*, 1196

Fox, D., et al. 2002, *GRB Circular Network*, 1334

Fox, D., et al. 2003, *The Astrophysical Journal*, **586**, L5-L8

Fox, D., et al. 2003, *GRB Circular Network*, 2323

Fruchter, A., et al. 2001, *GRB Circular Network*, 1268

Fruchter, A., et al. 2002, *GRB Circular Network*, 1781

Fynbo, J.P.U., et al. 2003, *GRB Circular Network*, 2327

Fynbo, J.P.U., et al. 2003, *GRB Circular Network*, 2345

Fynbo, J.P.U., et al. 2004, (astro-ph/0402240)

Galama, T.J., et al. 1998, *Nature*, **395**, 670

Garnavich, P., 2003, *GRB Circular Network*, 1848

Gilmore et al. 2003, *GRB Circular Network*, 2184

Gorosabel, J., et al. 2001, *GRB Circular Network*, 1224

Granot, J., Nakar, E., & Piran, T. 2003, *Nature*, **426**, 138-139

Groot, P.J. 1997, *IAU Circular*, 6584.1

Harris,M.J. & Share,G.H. 1998, *The Astrophysical Journal*, **494**, 724

Heise, J., in t Zand, J., Kippen, R. M., & Woods, P. M. 2001, in Proc. *2nd Rome Workshop on Gamma-ray Bursts in the Afterglow Era*, ed. E. Costa, F. Frontera, & J. Hjorth (Berlin: Springer), 16

Henden, A., 2002, *GRB Circular Network*, 1422

Huang, Y.F., et al. 2003, accepted by *The Astrophysical Journal*, (astro-ph/0309360)

Hurley, K., et al. 2002, *The Astrophysical Journal*, **567**, 447-453

Hurley, K., et al. 2002, *GRB Circular Network*, 1402

Hurley, K., et al. 2002, *GRB Circular Network*, 1407

Hurley, K., et al. 2002, *GRB Circular Network*, 1461

Jorgensen, S.F., et al. 2003, *GRB Circular Network*, 2344

Kato, D., et al. 2002, *GRB Circular Network*, 1363

Kato, D., et al. 2003, *GRB Circular Network*, 1825

Kato, D., et al. 2003, *GRB Circular Network*, 1830

Katz, J.I. 1994, *The Astrophysical Journal*, **422**, 248259

Kawai, N., et al. 2003, in AIP Conf. Proc. **662**, *Gamma Ray Burst and Afterglow Astronomy 2001*, ed. Ricker, G. & Vanderspek, R. (AIP Press: New York), 25

Kawai, N., et al. 2003, *GRB Circular Network*, 1816

Kawai, N., et al. 2003, *GRB Circular Network*,2412

Kinugasa, K., et al. 2001, *GRB Circular Network*, 1210

Kinugasa, K., et al. 2002, *GRB Circular Network*, 1749

Klebesadel, R., Strong, I., & Olson, R. 1973, *The Astrophysical Journal*, **182**, L85

Klebesadel, R., et al. 1980, IEEE Transactions on Geoscience and Remote Sensing, v. GE-18, 76-80

Kouveliotou, C., et al. 1993, *The Astrophysical Journal*, **413**, L101

Kulkarni, S., et al. 2002, *GRB Circular Network*, 1428

Lamb, D.Q., et al. 2002, submitted to *The Astrophysical Journal*, (astro-ph/0206151)

Lamb, D.Q., et al. 2002, *GRB Circular Network*, 1403

Lamb, D.Q., et al. 2004, *New Astronomy Reviews*, **48**, 423-430

Lamb, D.Q., et al. 2004, *New Astronomy Reviews*, **48**, 459-464

Levan, A., et al. 2002, *GRB Circular Network*, 1758

Levan, A., et al. 2003, *GRB Circular Network*, 1818

Li, W. D., et al. 2002, *GRB Circular Network*, 1405

Lipkin, Y.M., et al. 2004 *The Astrophysical Journal*, **606**, 381-394

Lubow, S. & Pollizzi, J. 1999, *Astronomical Data Analysis Software and Systems VIII*, ASP Conference Series, **172**, ed. D.M. Mehringer, R.L. Plante, & D.A. Roberts, 187

Mack, J., et al. 2003, ACS Data Handbook, v. 2.0, (Baltimore: STScI)

MacFadyen, A.I., & Woosley, S.E. 1999, *The Astrophysical Journal*, **524**, 262-289

Masetti, N., et al. 2003, *GRB Circular Network*, 1811

Masetti, N., et al. 2003, *GRB Circular Network*, 1823

Mazets, E.P. & Golenetskii, S.V. 1981, *Astrophysics and Space Science*, **75**, 47

McLeod, B., et al. 2002, *GRB Circular Network*, 1750

Meegan, C., et al. 1996, *The Astrophysical Journal, Supplement*, **106**, 65+

Mészáros, P. & Rees, M.J. 1993, *The Astrophysical Journal*, **405**, 278-284

Mészáros, P., Rees, M.J., & Wijers, R.A.M.J. 1998, *The Astrophysical Journal*, **499**, 301

Metzger, M.R., et al. 1997, *Nature*, **387**, 878

Miyazaki, S., et al. 2002, *Publications of the Astronomical Society of Japan*, **54**, 833

Monard, B. 2003, *GRB Circular Network*, 2324

Monard, B. 2003, *GRB Circular Network*, 2334

Monnelly, G., 2002, Ph.D. Thesis, M.I.T.

Monnelly, G., et al. 2003, in AIP Conf. Proc. **662**, *Gamma Ray Burst and Afterglow Astronomy 2001*, ed. Ricker, G. & Vanderspek, R. (AIP Press: New York), 49

Nakar, E., Piran, T., & Granot, J. 2003, *New Astronomy*, **8**, 495-505

Narayan, R., Paczynski, B., & Piran, T. 1992, *The Astrophysical Journal*, **395**, L83

Paciesas, W.S., et al. 1999, *The Astronomical Journal, Supplement*, **122**, 465-495

Preece, R. D., et al. 2000, *The Astrophysical Journal, Supplement*, **126**, 19

Price, P., et al. 2002, *GRB Circular Network*, 1316

Price, P., et al. 2003, *GRB Circular Network*, 2148

Price, P., et al. 2003, *GRB Circular Network*, 2150

Prigozhin, G., et al. 2003, *GRB Circular Network*, 2313

Quimby, R., McMahon, E., & Murphy, J. 2003, *GRB Circular Network*, 2298

Rees, M.J. & Mészáros, P. 1992, *Monthly Notices of the Royal Astronomical Society*, **258**, 41P

Reeves, J.N., et al. 2003, *Astronomy and Astrophysics*, **403**, 463-472

Rhoads, J.E. 1997, *The Astrophysical Journal*, **487**, L1

Rhoads, J.E. 1999, *The Astrophysical Journal*, **525**, 737

Ricker, G., et al. 2001, *GRB Circular Network*, 1194

Ricker, G., et al. 2002, *GRB Circular Network*, 1315

Ricker, G., et al. 2002, *GRB Circular Network*, 1399

Ricker, G., et al. 2003, in AIP Conf. Proc. **662**, *Gamma Ray Burst and Afterglow Astronomy 2001*, ed. Ricker, G. & Vanderspek, R. (AIP Press: New York), 3

Rykoff, E.S., et al. 2004, *The Astrophysical Journal*, **601**, 1013-1018

Saracco, P., et al. 2001, *GRB Circular Network*, 1205

Sari, R., Piran, T., & Narayan, R. 1998 *The Astrophysical Journal*, **497**, L17

Sari, R., Piran, T., & Halpern, J.P. 1999 *The Astrophysical Journal*, **519**, L17-L20

Schaefer, B.E., et al. 2003, *The Astrophysical Journal*, **588**, 387-399

Schecter, P., et al. 2003, in Proc. of the SPIE, **4837**, *Large Ground-based Telescopes.*, ed. Oschmann, J.M. & Stepp, L.M., 619-627

Shirasaki, Y., et al. 2003, *GRB Circular Network*, 2210

Shirasaki, Y., et al. 2003, *GRB Circular Network*, 2322

Šimon, V., et al. 2001, *Astronomy and Astrophysics*, **377**, 450-461

Smith, D.A., Akerlof, C.W., & Quimby, R. 2003, *GRB Circular Network*2338

Soderberg, A.M., et al. 2002, *GRB Circular Network*, 1460

Soderberg, A.M., et al. 2002, *GRB Circular Network*, 1554

Stanek, K. et al. 2003, *The Astrophysical Journal*, **591**, L17

Thomsen, B., et al. 2004, *Astronomy and Astrophysics*, **419**, L21-L25

Torii, K., et al. 2002, *GRB Circular Network*, 1387

van Paradijs, J., et al. 1997, *Nature*, **386**, 686

Vanden Berk, D., et al. 2001, *The Astronomical Journal*, **122**, 549-564

Vietri, M. & Stella, L. 1998, *The Astrophysical Journal*, **507**, L45-L48

Villasenor, J., et al. 2003, in AIP Conf. Proc. **662**, *Gamma Ray Burst and Afterglow Astronomy 2001*, ed. Ricker, G. & Vanderspek, R. (AIP Press: New York), 33

Vinter, C., et al. 2003, *GRB Circular Network*, 2335

Weidinger, M., et al. 2003, *GRB Circular Network*, 2196

Weisskopf, M. C. 2001, *Publications of the Astronomical Society of the Pacific*, **114**, 1

Woosley, S.E. 1993, *The Astrophysical Journal*, **405**, 273

Yamazaki, R., Ioka, K., & Nakamura, T. 2002, *The Astrophysical Journal*, **571**, L31-L35

Zhang, B. & Mészáros, P. 2003, *International Journal of Modern Physics A*, in press, (astro-ph/0311321)

Zhang, B., Woosley, S.E., & MacFadyen, A.I. 2003, *The Astrophysical Journal*, **586**, 356-371

Zhang, B., et al. 2004, *The Astrophysical Journal*, **601**, L119-L122

Appendix A

Acronym List

2MASS 2-Micron All Sky Survey

4Br 4th BATSE Catalog (revised)

ACIS Advanced CCD Imaging System

ACS Advanced Camera for Surveys

AGN Active Galactic Nucleus

BATSE Burst and Transient Source Experiment

BH Black Hole

CCD Charge Coupled Device

CGRO Compton Gamma-Ray Observatory

CXO Chandra X-Ray Observatory

DSS Digitized Sky Survey

DXRB Diffuse X-ray Background

FOV Field Of View

FRED Fast Rise Exponential Decay

FREGATE French Gamma-ray Telescope

FWHM Full Width at Half Maximum

FWZM Full Width at Zero Maximum

GCN GRB Coordinates Network

GRB Gamma-ray Burst

HEG High Energy Grating

HETE High Energy Transient Explorer

HST Hubble Space Telescope

IDL Interactive Data Language

IPN Inter-Planetary Network

IR Infra-Red

IRAF Interactive Reduction and Analysis Facility

LDSS2 Low Dispersion Survey Spectrograph

MagIC Magellan Instant Camera

MAST Multimission Archive at Space Telescope Science Institute

NICMOS Near Infrared Camera and Multi Object Spectrometer

NIR Near Infra-Red

NS Neutron Star

PGS Primary Ground Station

POS POSition histogram data

S/N Signal to Noise Ratio

SAA South Atlantic Anomaly

SGR Soft-Gamma Repeater

SN Supernova

SOD Seconds of Day

STIS Space Telescope Imaging Spectrograph

STSci Space Telescope Science Institute

SXC Soft X-ray Camera

ToO Target of Oppurtunity

USNO United States Naval Observatory

VHF Very High Frequency

WXM Wide Field X-ray Monitor

XRB X-ray Burst

XRF X-ray Flash